Dead Sea Warming and the Origin of Salt Giants

Emmanuel Guillerm^{1,2}*, Tim K. Lowenstein², Véronique Gardien³, Fabian Bärenbold^{4,5}, Damien Bouffard^{5,4}, Achim Brauer¹, Frédéric Caupin⁶

¹GFZ Helmholtz Centre for Geosciences, Section 4.6, Working Group "Terrestrial Climate Archives"

²Department of Earth Sciences, Binghamton University

³ Université Claude Bernard Lyon 1, LGL-TPE, UMR CNRS 5276, ENS Lyon, 69622 Villeurbanne Cedex France

⁴Institute of Earth Surface Dynamics, University of Lausanne, Lausanne, Switzerland

⁵Eawag, Swiss Federal Institute of Aquatic Science and Technology, Surface Waters –

Research and Management, Kastanienbaum, Switzerland

⁶Institut Lumière Matière, Université Claude Bernard Lyon 1, CNRS, Institut Universitaire de France

*Corresponding author: emmanuel.guillerm@gfz.de; emmanuel.guillerm@outlook.fr

Peer review status:

This is a non-peer-reviewed preprint submitted to EarthArXiv.

Orcid of contact author:

https://orcid.org/0000-0002-2725-9229

Abstract

Episodically, vast seas on Earth partly dried out, leaving deposits called "salt giants". Recently, in addition to well-documented accelerated level decline and salt precipitation, the Dead Sea has suffered severe warming. The mechanisms underlying this warming and the formation of salt giants remain unresolved. Here we propose a physical model of hypersaline waterbodies that reproduces Dead Sea observations and projects extreme warming: within the next 200 years, water temperatures will rise twice as much as anthropogenic air warming. Applied to the Messinian Salinity Crisis, 5.5 Ma, our model reveals that a positive feedback between water temperature increase and water level lowering drove massive Mediterranean Sea warming and drawdown and best explains the accumulation of highly soluble minerals under temperate humid conditions.

Introduction

Salt giants are evaporite deposits on the scale of millions of cubic kilometers, formed episodically throughout the Phanerozoic (Hay et al., 2006). The most recent example formed in less than 100 kyr after isolation of the Mediterranean Sea from the Atlantic, during "Stage 2" of the Messinian Salinity Crisis, 5.5 Ma (Krijgsman et al., 1999; Roveri et al., 2014), as the result of a near-complete desiccation (Hsü et al., 1973) or partial drawdown (Christeleit et al., 2015; Clauzon et al., 1996; Hardie & Lowenstein, 2004).

The environmental conditions required for salt-giant formation remain hotly debated. Many evaporite deposits contain highly soluble salts such as magnesium and potassium chlorides, which require brines with very low H_2O activity (a_w) —the measure of how much the chemical potential of water in solution differs from pure water $(a_w = 1)$. In an evaporating hypersaline brine, salinity increases and a_w decreases, until evaporation ceases when a_w falls below the relative humidity of the overlying air (Kinsman, 1976; Zilberman et al., 2017), assuming equal air and water temperatures (Oroud, 2019; Salhotra et al., 1985). For this reason, the presence of these highly soluble minerals has been interpreted as evidence for extremely arid climates (Chaboureau et al., 2012; Kinsman, 1976; Schreiber & El Tabakh, 2000; Warren, 2010). Paleotemperature reconstructions further suggest brine temperatures well above 50 °C in many evaporite deposits (Wang & Lowenstein, 2017), pointing to unusually hot settings. The apparent scarcity of such hot-arid climate conditions has led some studies to invoke alternative, non-evaporative drivers of salt-giant formation, e.g. hydrothermal processes (Chaboureau et al., 2012; Debure et al., 2019; Hovland et al., 2006; Scribano et al., 2017; Wang & Lowenstein, 2017).

As the only deep lake saturated with respect to halite (Sirota et al., 2016), the Dead Sea (Fig. 1) is a unique natural laboratory for studying the hypersaline waterbodies that formed salt giants (Meiburg & Lensky, 2025). Since 1979, when the lake switched from meromixis to holomixis (i.e. from permanently to seasonally stratified) and became saturated with respect to halite (Steinhorn, 1983; Steinhorn et al., 1979), the Dead Sea has experienced extreme water warming. In 2012–2015, the upper water layer—the epilimnion—had a mean annual temperature of 28.5 °C (Arnon et al., 2016), 1.8 °C higher than in 1980–1984 (Stanhill, 1990), a warming rate comparable to that of the air (Fig. 2) and 60% higher than the regional lake surface water warming rate (~0.35 °C/decade) (Tong et al., 2023). The temperature rise of the deep water layer—the hypolimnion—is even more striking: from ~21.5 °C in 1979 to 24.3 °C in the 2010s

(Fig. 2), an average rate 10 times that of deep lake waters worldwide (0.06 °C/decade) (Pilla et al., 2020).

The causes of this rapid warming remain unresolved. Several studies estimated surface fluxes and storage of heat in the Dead Sea (Lensky et al., 2005; Oroud, 2023; Stanhill, 1990, 1994) but covered only short time intervals of the late 20th century and/or assumed stationary climate. However, several key factors affecting heat fluxes have changed significantly since the 1970s: lake level has dropped by ~40 m (Fig. S1), air temperature has increased by ~1.8 °C, relative humidity peaked in the 1980s–1990s and has declined since, brine H₂O activity has dropped by ~0.03 (Fig. S2), and the lake experienced two short returns to meromixis since 1979 following exceptional floods.

One of the peculiarities of the Dead Sea heat budget is the large magnitude of diapycnal (i.e. vertical) fluxes of heat from the epilimnion to the hypolimnion, due to enhancement by double-diffusive (DD) salt fingering (Anati & Stiller, 1991; Arnon et al., 2016). DD salt fingering results from the characteristic summer stratification of deep holomictic hypersaline lakes, whereby the warm, salty epilimnion overlies the cooler, slightly fresher hypolimnion. As heat diffuses faster than salt, sinking salt fingers lose buoyancy and continue downward, transporting heat and salt across the interface (Radko, 2013). The consequence of these fluxes on the long-term temperature evolution of the Dead Sea have not been investigated.

To investigate Dead Sea warming and its implications for understanding salt giant genesis, we constructed a thermal model of deep hypersaline lakes (see *Materials and Methods*). This model employs a physically-based framework to quantify air-water interface heat fluxes and diapycnal heat transport. The model simulates lake water temperature and level by solving a system of ordinary differential equations, either for two distinct water layers during holomictic stratified seasons and meromictic periods, or for a single mixed layer during holomictic mixing seasons. Heat fluxes across the air-water interface are computed from surface water properties and interpolated monthly climatic timeseries. Diapycnal heat fluxes are modeled as an effective diffusion process with separate diffusivity terms for turbulence (mainly related to mixing by wave action) and double diffusion. We calibrated both terms using monthly-resolved epilimnion and hypolimnion temperature observations in the Dead Sea from a limited period, 2012–2015 (Fig. S3), less than 10% of the length of the model validation period 1979–2019. Lake level change is computed from evaporation and inflow rates. The surface area and volume of each

water layer vary over time and are derived from lake level, bathymetry, and a fixed thermocline depth (Fig. S1). Our model reveals that holomictic hypersaline waterbodies under water deficit experience warming and shrinkage in a positive feedback loop, amplifying water level drop and precipitation of highly soluble minerals even under conditions of elevated relative humidity.

Results and Discussion

Model validation: the Dead Sea, 1979–2019

To evaluate model performance, we ran a baseline simulation of the Dead Sea from 1979 to 2019 using monitored climate and surface water density timeseries (see *Materials and Methods*). In this simulation and in the following sensitivity simulations, lake level is prescribed using observations (Fig. S1).

Simulated epilimnion and hypolimnion temperatures are in excellent agreement with observations. Statistical measures yield little bias and deviation between model and data, and simulated warming between the 20th century meromictic Dead Sea and the 2010s, 1.6 °C for the epilimnion and 2.8 °C for the hypolimnion, are in line with observations (Fig. 3). Moreover, the model accurately captures the contrasting dynamical responses of epilimnetic and hypolimnetic temperatures, which exhibit sinusoidal and sawtooth patterns respectively during holomixis and amplified and muted thermal variability respectively during meromixis (Figs 3, S3). As a side product, the model predicts annual overturn dates, which average December 13 (range: Nov 20–Dec 27), consistent with observations (Fig. S4). Modeled net air—water heat flux also agrees closely with observations (Fig. S5).

Interestingly, the ratio of the calibrated DD heat diffusivity to molecular heat diffusivity is 33, which is commensurate with the heat flux ratio ~30 obtained by Navier-Stokes numerical experiments reproducing the summer holomictic Dead Sea (Ouillon et al., 2019).

Overall, the strong agreement with observations over a validation period more than 10 times longer than calibration period, supports model reliability and justifies its application in sensitivity and scenario simulations.

Combined impact of lake level and air temperature

To assess the total impact of recent air warming and lake level decline, we ran a sensitivity simulation with no air warming and no lake level decline. Compared to the baseline, two changes

were made: (i) air temperature was held constant at the 1950–1978 average annual cycle and (ii) lake level was fixed at -400.3 m asl (1979 level), hence constant H₂O activity (0.674) and suppressed DD heat flux (due to stable epilimnion salinity during stratified season).

Epilimnion temperature (Fig. 3A) remains stable around an annual mean of 26.3 °C, close to the 20th century surface water temperature under meromixis (26.5 °C). Seasonal extremes remain stable around 21.5–33 °C. By 2010–2019, the epilimnion is up to 2.8 °C cooler than in the baseline simulation, particularly in winter.

Hypolimnion temperature (Fig. 3B) stays within the 21.5–22 °C range, close to 20th century deep water temperature under meromixis (21.5 °C). We attribute the 0.5 °C decrease from the 1980s to the 2010s to the decrease in relative humidity (Fig. S2), which enhances evaporative cooling.

The temperature stability of both water layers in this sensitivity simulation confirms that air warming and lake level decline are the drivers of observed temperature increases. It also means the 1979 transition to holomixis alone did not significantly alter the lake's thermal equilibrium.

Separate impacts of lake level and air temperature

To isolate the respective contributions of air warming and lake level decline, we conducted two additional sensitivity simulations. Compared to the baseline, the only change is that either air temperature was held constant at the 1950–1978 average annual cycle, or lake level was fixed at the 1979 value.

In the simulation with fixed air temperature annual cycle, by the 2010s mean epilimnion temperature is 26.8 °C (Fig. 3A) and mean hypolimnion temperature is 23 °C (Fig. 3B). Comparison with the baseline simulation reveals that, by the 2010s, air warming contributed 1.3 °C to both epilimnion and hypolimnion warmings. Comparison with the simulation with no air warming and no lake level decline reveals that, by the 2010s, lake level decline contributed 0.5 °C to epilimnion warming and 1.5 °C to hypolimnion warming. These values are confirmed by the simulation with fixed lake level only (not shown).

We first explore the mechanism by which lake level decline induces water warming in holomictic conditions. For the hypolimnion, two main processes are involved. (i) During the winter mixed season, lower H₂O activity limits evaporative cooling. (ii) During the stratified season, increased salinity difference and volume ratio between the epilimnion and hypolimnion amplify diapycnal fluxes. For the epilimnion, in the stratified season lake level decline induces

water cooling due to diapycnal fluxes, but this is more than offset by the warming effect of lake level decline on the mixed waterbody in winter: the annual average impact of lake level decline on surface water temperature is therefore positive.

We now consider the impact of air warming on water temperature. For +1.8 °C of air warming on annual average, our sensitivity simulations reveal a warming of 1.3 °C in each water layer, hence a warming rate of 0.72 °C per 1 °C of air warming. This epilimnetic response aligns with the global lake averages (Tong et al., 2023). Conversely, this hypolimnetic response contrasts with the more complex, more indirect, and much weaker deep water–atmosphere coupling in deep freshwater lakes (Livingstone, 1993; Pilla et al., 2020), as best illustrated by the absence of recent hypolimnion warming in lake Kinneret (Rimmer et al., 2011), a deep warm holomictic freshwater lake close to the Dead Sea.

Two processes can explain the strong hypolimnion response to air warming in the Dead Sea. First, compared to other lakes, diapycnal flux during the stratified period is enhanced by double diffusion. This process transfers heat from the epilimnion to the hypolimnion and thereby enhances the deep water–atmosphere connection. Second and most importantly, we suggest the long mixed period (3–4 months), with strong convection due to the large positive water–air temperature difference that supports surface cooling (Anati & Stiller, 1991), provides a strong deep water–atmosphere connection. The results of our simulations in which only the temperature of the air of one month is fixed (supplementary text) show that ~90% of air warming-driven hypolimnion warming occurs between November and March, thus confirming the importance of the winter mixed period in the deep water–atmosphere connection.

Given ongoing lake level decline and air warming, and the amplified lake temperature response to these changes as demonstrated by our simulations, the question arises: how will the Dead Sea evolve in the coming centuries?

Projected Dead Sea warming and shrinkage

To estimate the future evolution of the Dead Sea, we ran a projection simulation from 2019 to 2600, accounting for both greenhouse gas-driven air warming and anthropogenic lake level decline. Compared to the baseline simulation, we implemented the following changes: (i) air temperature increased with the current local anthropogenic warming rate of +0.045 °C yr⁻¹ capped at +10 °C to simulate high-emission scenario SSP3 7.0 of the IPCC (IPCC, 2021); (ii)

relative humidity, wind speed and insolation were held constant at their 1950–1978 average annual cycle; and (iii) H₂O activity was dynamically computed based on a published relationship with lake level (Zilberman et al., 2017).

According to the projection simulation, the lake will undergo massive, water-column-wide warming. Both epilimnion and hypolimnion temperatures will rise at nearly double the rate of air temperature until 2200, and continue rising after 2200 despite the end of anthropogenic air warming (Fig. 4A). By 2600, epilimnion and hypolimnion will oscillate annually in the ranges 40.5–54 °C and 40.5–42.5 °C, respectively. The surface water–air temperature difference will reach a maximum in January (+13 °C) and a minimum in May (+7 °C). This excess water warming relative to the air primarily owes to the reduction of evaporative cooling linked to the decrease in H₂O activity. This strong warming effect of reduced H₂O activity is further supported by observations in the hypersaline ponds surrounding the Dead Sea. There, a clear H₂O activity–water temperature inverse relationship is observed, and summer water temperatures in the range ~40–50 °C have been measured in the most concentrated brines (~6–16 °C above mean temperature of the warmest month) (Oroud, 1995) (Fig. S8).

Still according to the projection simulation, the lake level drop will considerably exceed previous estimates. The lake level will reach -517 m asl when H₂O activity equals relative humidity (~0.41), which is in close agreement with previously estimated equilibrium lake level under no inflow and no potash production assumptions (Krumgalz et al., 2000; Zilberman et al., 2017). However, in our projection the lake will keep declining thereafter until equilibrium is reached around 2600 with a level of -580 m asl and H₂O activity of 0.26. This lower equilibrium level stems from our model accounting for water and air temperatures in the calculation of evaporation. As water–air vapor pressure difference increases exponentially with water–air temperature difference, evaporation continues even when H₂O activity is below ambient relative humidity. This effect is maximal right after the overturn, in December–January, when the surface water–air temperature difference peaks due to the large thermal inertia of the mixed waterbody.

This "temperature effect" highlights a hitherto unidentified positive feedback loop of brine warming and shrinkage: water warming induces more evaporation, which decreases H₂O activity, thereby reducing evaporative cooling and leading to more water warming. In deep brine bodies, this positive feedback loop is further amplified by diapycnal fluxes, which store all the more heat in the hypolimnion as summer evaporation rate is high.

As the temperature effect allows substantially faster and more extensive waterbody shrinkage, these results raise a broader question: did similar thermal-evaporative feedbacks occur in ancient hypersaline systems that formed large evaporite deposits? And to what extent does lapse rate amplify water warming in the case of kilometric water level drops?

Warming and shrinkage of isolated seas

Building on the findings from the Dead Sea, we applied our modeling approach to simulate Stage 2 of the Messinian Salinity Crisis in the eastern Mediterranean. The simulation began with a brine-filled basin at -400 m asl, just below the depth of the Strait of Sicily, and used a basin hypsometry derived from our digital elevation model of the eastern Mediterranean basin (Fig. S1). The brine composition started at halite saturation, following recent findings that the brine was close to halite saturation just before Stage 2 (Bigi et al., 2022). Composition then evolved with water volume, as dictated by our chemical equilibrium simulation of Messinian seawater evaporation (see *Materials and Methods*). Air temperature followed the Dead Sea's 1950–1978 annual cycle, adjusted based on lapse rate. Surface air pressure was adjusted to water level using a hydrostatic correction (Minzner et al., 1959). Latitude (34 °N), relative humidity (65%), wind speed (6 m s⁻¹), and clearness index (60%) were held constant at modern values. The simulation was run for 9000 years under holomictic conditions. The simulation is not intended as a detailed reconstruction, given some important simplifications and uncertainties: uncertain initial salinity, lack of basin compartmentalization, absence of inflow, and use of modern climate and hypsometry. Instead, it tests whether the same thermal-evaporative feedbacks at play in the Dead Sea could operate in a larger basin and over longer timescales.

According to the simulation, the eastern Mediterranean Sea underwent a ~20 °C warming during Stage 2, which is comparable to the projected Dead Sea warming (Fig. 4B). This massive warming occurred despite the absence of anthropogenic air warming, and is coeval with a 14 °C lapse rate-driven air warming. During the first 1500 years of drawdown, water warming closely followed air warming. After that, as the drop of the H₂O activity of the brine accelerated, water temperatures rose faster than air temperature. After ~8,000 years, epilimnion and hypolimnion reached an equilibrium, oscillating annually in the ranges 41–54 °C and 41–41.5 °C, respectively. The surface water–air temperature difference reached a maximum in January (+9 °C) and a minimum in May (+5 °C).

Still according to the simulation, the eastern Mediterranean Sea dropped by 2500 m during Stage 2, reaching equilibrium at ~-2900 m asl and H₂O activity 0.47 after ~8000 yr. As projected for the Dead Sea, the simulated contribution of winter evaporation to the water level drop increased throughout the drawdown, and, due to the temperature effect, water level kept declining when H₂O activity became lower than relative humidity—in this case by an additional ~600 m. The simulated level drop is somewhat larger than the recently reconstructed ~2 km level drop based on geochemical evidence from the far eastern part of the basin (Aloisi et al., 2024), probably due to the simulation simplifications and uncertainties mentioned earlier. The simulated drawdown duration is in line with previous modeling- (Meijer & Krijgsman, 2005) and observation-based (Manzi et al., 2012) estimates for Stage 2.

Crucially, saturation levels of potassium and magnesium salts were all reached in the simulation at H₂O activities lower than relative humidity. Our results thus demonstrate that the observed occurrence of these highly soluble salts in the Messinian sedimentary record (Lugli et al., 1999; Manzi et al., 2012) is compatible with modern Mediterranean conditions of air temperature and relative humidity.

Our model provides a physical explanation for the extremely high brine paleotemperatures and low brine H₂O activity reconstructed from numerous ancient evaporite deposits. It shows that, once disconnected from the ocean, vast hypersaline seas can warm by several tens of degrees through lapse rate-driven air warming, reduced evaporative cooling, and enhanced diapycnal heat flux. This warming amplifies evaporation, accelerating and deepening water level decline, and enables the precipitation of highly soluble salt that would otherwise remain undersaturated under temperate—humid conditions.

As emerging paleothermometry techniques now allow accurate reconstructions of brine temperatures from halite fluid inclusions (Arnuk et al., 2024; Brall et al., 2022; Guillerm et al., 2020, 2025; Olson et al., 2023), our model predictions can be directly tested, with an expected upsection increase in paleobrine temperature.

References and Notes

Aloisi, G., Moneron, J., Guibourdenche, L., Camerlenghi, A., Gavrieli, I., Bardoux, G., Agrinier, P., Ebner, R., & Gvirtzman, Z. (2024). Chlorine isotopes constrain a major drawdown of the

- Mediterranean Sea during the Messinian Salinity Crisis. *Nature Communications*, 15(1), 9671.
- American Meteorological Society. (2024). *Virtual Potential Temperature*. Glossary of Meteorology. https://glossary.ametsoc.org/wiki/Virtual potential temperature
- Anati, D. A. (1996). The hydrography of a hypersaline lake. *Oxford Monographs on Geology and Geophysics*, *36*(1), 89–103.
- Anati, D. A., & Stiller, M. (1991). The post- 1979 thermohaline structure of the Dead Sea and the role of double-diffusive mixing. *Limnology and Oceanography*, *36*(2), Article 2. https://doi.org/10.4319/lo.1991.36.2.0342
- Arnon, A., Selker, J. S., & Lensky, N. G. (2016). Thermohaline stratification and double diffusion diapycnal fluxes in the hypersaline Dead Sea. *Limnology and Oceanography*, 61(4), Article 4. https://doi.org/10.1002/lno.10285
- Arnuk, W. D., Guillerm, E., Lowenstein, T. K., Krüger, Y., Olson, K. J., Lensky, N. G., & Brauer, A. (2024). Nucleation-assisted microthermometry: A novel application to fluid inclusions in halite. *Chemical Geology*, 667, 122318. https://doi.org/10.1016/j.chemgeo.2024.122318
- Ashin, K., Girishkumar, M. S., Joseph, J., D'Asaro, E., Sureshkumar, N., Sherin, V. R., Murali, B., Thangaprakash, V. P., Rao, E. P. R., & Shenoi, S. S. C. (2022). Double Diffusion in the Arabian Sea during Winter and Spring. *Journal of Physical Oceanography*, *52*(6), 1205–1231. https://doi.org/10.1175/JPO-D-21-0186.1
- Atwater, M. A., & Brown, P. S. (1974). Numerical Computations of the Latitudinal Variation of Solar Radiation for an Atmosphere of Varying Opacity. *Journal of Applied Meteorology and Climatology*, *13*(2), Article 2. https://doi.org/10.1175/1520-0450-13.2.289
- Ben Dor, Y., Flax, T., Levitan, I., Enzel, Y., Brauer, A., & Erel, Y. (2021). The paleohydrological implications of aragonite precipitation under contrasting climates in the endorheic Dead Sea and its precursors revealed by experimental investigations. *Chemical Geology*, 576, 120261. https://doi.org/10.1016/j.chemgeo.2021.120261
- Berger, A. (1978). Long-term variations of daily insolation and Quaternary climatic changes. *Journal of the Atmospheric Sciences*, 35(12), Article 12.

- Beyth, M. (1980). Recent evolution and present stage of Dead Sea brines. In *Developments in Sedimentology* (Vol. 28, pp. 155–166). Elsevier.
- Beyth, M., Gavrieli, I., Anati, D., & Katz, O. (1993). Effects of the December 1991-May 1992 floods on the Dead Sea vertical structure. *Israel J. Earth Sci.*, 42(1), Article 1.
- Beyth, M., Gertman, I., Weinstein, R., & Gavrieli, I. (1998). End brine mixing in the Dead Sea (July 20, 1998) (No. GSI/30/98). Geological Survey of Israel.
- Bigi, D., Lugli, S., Manzi, V., & Roveri, M. (2022). Are fluid inclusions in gypsum reliable paleoenvironmental indicators? An assessment of the evidence from the Messinian evaporites. *Geology*, *50*(4), 454–459.
- Brall, N. S., Gardien, V., Ariztegui, D., Sorrel, P., Guillerm, E., & Caupin, F. (2022).
 Reconstructing lake bottom water temperatures and their seasonal variability in the Dead Sea
 Basin during MIS5e. *The Depositional Record*, 8(2), Article 2.
 https://doi.org/10.1002/dep2.185
- Brennan, S. T., Lowenstein, T. K., & Cendón, D. I. (2013). The major-ion composition of Cenozoic seawater: The past 36 million years from fluid inclusions in marine halite. *American Journal of Science*, 313(8), Article 8.
- Brouwer, D., & Clemence, G. M. (2013). Methods of Celestial Mechanics. Elsevier.
- Brutsaert, W. (1982). Evaporation into the Atmosphere: Theory, History and Applications. Springer Netherlands.
- Chaboureau, A.-C., Donnadieu, Y., Sepulchre, P., Robin, C., Guillocheau, F., & Rohais, S. (2012). The Aptian evaporites of the South Atlantic: A climatic paradox? *Climate of the Past*, 8(3), 1047–1058.
- Christeleit, E. C., Brandon, M. T., & Zhuang, G. (2015). Evidence for deep-water deposition of abyssal Mediterranean evaporites during the Messinian salinity crisis. *Earth and Planetary Science Letters*, 427, 226–235. https://doi.org/10.1016/j.epsl.2015.06.060
- Clauzon, G., Suc, J.-P., Gautier, F., Berger, A., & Loutre, M.-F. (1996). Alternate interpretation of the Messinian salinity crisis: Controversy resolved? *Geology*, 24(4), 363–366.

- Coddington, O., Lean, J. L., Pilewskie, P., Snow, M., & Lindholm, D. (2016). A Solar Irradiance Climate Data Record. *Bulletin of the American Meteorological Society*, *97*(7), Article 7. https://doi.org/10.1175/BAMS-D-14-00265.1
- Copernicus Climate Change Service (C3S). (2022). *ERA5-Land monthly averaged data from* 1950 to present. Copernicus Climate Change Service (C3S) Climate Data Store (CDS). [Data set]. https://doi.org/10.24381/cds.68d2bb30
- Crawford, T. M., & Duchon, C. E. (1999). An Improved Parameterization for Estimating Effective Atmospheric Emissivity for Use in Calculating Daytime Downwelling Longwave Radiation. *Journal of Applied Meteorology and Climatology*, *38*(4), Article 4. https://doi.org/10.1175/1520-0450(1999)038%253C0474:AIPFEE%253E2.0.CO;2
- Debure, M., Lassin, A., Marty, N. C., Claret, F., Virgone, A., Calassou, S., & Gaucher, E. C. (2019). Thermodynamic evidence of giant salt deposit formation by serpentinization: An alternative mechanism to solar evaporation. *Scientific Reports*, *9*(1), 11720.
- Dilley, A. C., & O'brien, D. M. (1998). Estimating downward clear sky long-wave irradiance at the surface from screen temperature and precipitable water. *Quarterly Journal of the Royal Meteorological Society*, *124*(549), 1391–1401.
- Fairall, C. W., Bradley, E. F., Godfrey, J. S., Wick, G. A., Edson, J. B., & Young, G. S. (1996).
 Cool-skin and warm-layer effects on sea surface temperature. *Journal of Geophysical Research: Oceans*, 101(C1), 1295–1308.
- Gavrieli, I., Beyth, M., & Gertman, I. (2000). *End brine mixing in the Dead Sea (September 6-7, 1999)* (No. GSI/3/2000). Geological Survey of Israel.
- Gavrieli, I., Beyth, M., Weinstein, R., & Anati, D. A. (1996). The end of the latest meromictic period in the Dead Sea and its effect on the mixing of the end brines in summer 1995 (August 7-9, 1995) (No. GSI/3/96). Geological Survey of Israel.
- Gavrieli, I., Gertman, I., & Beyth, M. (2001). *End brine mixing in the Dead Sea (August 21-22, 2000)* (No. GSI/8/2001). Geological Survey of Israel.
- Gavrieli, I., Weinstein, R., & Beyth, M. (1998). End brine mixing in the Dead Sea (August 11-13, 1997) (No. GSI/7/98). Geological Survey of Israel.

- Gertman, I., & Hecht, A. (2002). The Dead Sea hydrography from 1992 to 2000. *Journal of Marine Systems*, 35(3), Article 3. https://doi.org/10.1016/S0924-7963(02)00079-9
- Gertman, I., Kress, N., Katsenelson, B., & Zavialov, P. (2010). Equations of state for the Dead Sea and Aral Sea: Searching for common approaches. IOLR.
- Guillerm, E., Gardien, V., Ariztegui, D., & Caupin, F. (2020). Restoring Halite Fluid Inclusions as an Accurate Palaeothermometer: Brillouin Thermometry Versus Microthermometry. *Geostandards and Geoanalytical Research*, 44(2), Article 2. https://doi.org/10.1111/ggr.12312
- Guillerm, E., Gardien, V., Waldmann, N. D., Brall, N. S., Ariztegui, D., Schwab, M. J., Neugebauer, I., Lach, A., & Caupin, F. (2023). Reconstruction of Dead Sea lake level and mass balance back to 237 ka BP using halite fluid inclusions. *Quaternary Science Reviews*, 303, 107964. https://doi.org/10.1016/j.quascirev.2023.107964
- Guillerm, E., Lowenstein, T. K., Gardien, V., Brauer, A., Krüger, Y., Arnuk, W. D., & Caupin, F. (2025). A Physical Model for Accurate Paleotemperature Reconstruction From Fluid Inclusions in Halite. *American Journal of Science*, 325, Article 7. https://doi.org/10.2475/001c.130836
- Hamdani, I., Assouline, S., Tanny, J., Lensky, I. M., Gertman, I., Mor, Z., & Lensky, N. G. (2018). Seasonal and diurnal evaporation from a deep hypersaline lake: The Dead Sea as a case study. *Journal of Hydrology*, *562*, 155–167. https://doi.org/10.1016/j.jhydrol.2018.04.057
- Hardie, L. A., & Lowenstein, T. K. (2004). Did the Mediterranean Sea dry out during the Miocene? A reassessment of the evaporite evidence from DSDP Legs 13 and 42A cores. *Journal of Sedimentary Research*, 74(4), 453–461.
- Hay, W. W., Migdisov, A., Balukhovsky, A. N., Wold, C. N., Flögel, S., & Söding, E. (2006). Evaporites and the salinity of the ocean during the Phanerozoic: Implications for climate, ocean circulation and life. *Palaeogeography, Palaeoclimatology, Palaeoecology*, 240(1), 3–46. https://doi.org/10.1016/j.palaeo.2006.03.044
- Hecht, A., & Gertman, I. (2003). Dead Sea meteorological climate. In *Fungal Life in the Dead Sea* (E. Nevo, A. Oren and S. P. Wasser, pp. 68–114). A.R.G. Gantner.

- Hovland, M., Rueslåtten, H. G., Johnsen, H. K., Kvamme, B., & Kuznetsova, T. (2006). Salt formation associated with sub-surface boiling and supercritical water. *Marine and Petroleum Geology*, 23(8), 855–869.
- Hsü, K. J., Ryan, W. B. F., & Cita, M. B. (1973). Late Miocene Desiccation of the Mediterranean. *Nature*, 242(5395), 240–244. https://doi.org/10.1038/242240a0
- Inoue, R., Yamazaki, H., Wolk, F., Kono, T., & Yoshida, J. (2007). An Estimation of Buoyancy Flux for a Mixture of Turbulence and Double Diffusion. *Journal of Physical Oceanography*, *37*(3), 611–624. https://doi.org/10.1175/JPO2996.1
- IOLR. (2021). *Israel Oceanographic and Limnologic Research (IOLR)* [Website]. Monitoring of the Dead Sea. https://isramar.ocean.org.il/isramar2009/DeadSea/
- IPCC. (2021). Climate Change 2021: The Physical Science Basis. Contribution of Working Group I to the Sixth Assessment Report of the Intergovernmental Panel on Climate Change: Vol. In Press. Cambridge University Press. https://doi.org/10.1017/9781009157896
- Israel Hydrological Service. (2020). Dead Sea lake level data, 1976–2020 [Data set].
- Jiménez, P. A., Dudhia, J., González-Rouco, J. F., Navarro, J., Montávez, J. P., & García-Bustamante, E. (2012). A revised scheme for the WRF surface layer formulation. *Monthly Weather Review*, 140(3), 898–918.
- Kasten, F. (1965). A new table and approximation formula for the relative optial air mass. *Archiv Für Meteorologie, Geophysik Und Bioklimatologie, Serie B*, *14*(2), Article 2. https://doi.org/10.1007/BF02248840
- Kinsman, D. J. J. (1976). Evaporites; relative humidity control of primary mineral facies. *Journal of Sedimentary Research*, 46(2), 273–279. https://doi.org/10.1306/212F6F37-2B24-11D7-8648000102C1865D
- Kishcha, P., Pinker, R. T., Gertman, I., Starobinets, B., & Alpert, P. (2018). Observations of positive sea surface temperature trends in the steadily shrinking Dead Sea. *Natural Hazards and Earth System Sciences*, *18*(11), Article 11. https://doi.org/10.5194/nhess-18-3007-2018
- Krijgsman, W., Hilgen, F. J., Raffi, I., Sierro, F. J., & Wilson, D. S. (1999). Chronology, causes and progression of the Messinian salinity crisis. *Nature*, 400(6745), 652–655. https://doi.org/10.1038/23231

- Krumgalz, B. S., Hecht, A., Starinsky, A., & Katz, A. (2000). Thermodynamic constraints on Dead Sea evaporation: Can the Dead Sea dry up? *Chemical Geology*, *165*(1–2), 1–11.
- Kunze, E. (2003). A review of oceanic salt-fingering theory. *Progress in Oceanography*, *56*(3), 399–417. https://doi.org/10.1016/S0079-6611(03)00027-2
- Lensky, N. G., Y. Dvorkin, Lyakhovsky, V., Gertman, I., & Gavrieli, I. (2005). Water, salt, and energy balances of the Dead Sea. *Water Resources Research*, 41(12), Article 12. https://doi.org/10.1029/2005WR004084
- Livingstone, D. M. (1993). Temporal structure in the deep-water temperature of four Swiss lakes: A short-term climatic change indicator? *SIL Proceedings*, 1922-2010, 25(1), Article 1. https://doi.org/10.1080/03680770.1992.11900062
- Lugli, S., Schreiber, B. C., & Triberti, B. (1999). Giant polygons in the Realmonte Mine (Agrigento, Sicily); evidence for the desiccation of a Messinian halite basin. *Journal of Sedimentary Research*, 69(3), 764–771.
- Manzi, V., Gennari, R., Lugli, S., Roveri, M., Scafetta, N., & Schreiber, B. C. (2012). High-frequency cyclicity in the Mediterranean Messinian evaporites: Evidence for solar–lunar climate forcing. *Journal of Sedimentary Research*, 82(12), 991–1005.
- Meiburg, E., & Lensky, N. G. (2025). Fluid Mechanics of the Dead Sea. *Annual Review of Fluid Mechanics*, 57(Volume 57, 2025), 167–196. https://doi.org/10.1146/annurev-fluid-031424-101119
- Meijer, P. Th., & Krijgsman, W. (2005). A quantitative analysis of the desiccation and re-filling of the Mediterranean during the Messinian Salinity Crisis. *Earth and Planetary Science Letters*, 240(2), 510–520. https://doi.org/10.1016/j.epsl.2005.09.029
- Merryfield, W. J., Holloway, G., & Gargett, A. E. (1999). A Global Ocean Model with Double-Diffusive Mixing. *Journal of Physical Oceanography*, *29*(6), 1124–1142. https://doi.org/10.1175/1520-0485(1999)029%253C1124:AGOMWD%253E2.0.CO;2
- Metzger, J., Nied, M., Corsmeier, U., Kleffmann, J., & Kottmeier, C. (2018). Dead Sea evaporation by eddy covariance measurements vs. Aerodynamic, energy budget, Priestley–Taylor, and Penman estimates. *Hydrology and Earth System Sciences*, 22(2), 1135–1155.

- Meyers, T. P., & Dale, R. F. (1983). Predicting Daily Insolation with Hourly Cloud Height and Coverage. *Journal of Applied Meteorology and Climatology*, *22*(4), Article 4. https://doi.org/10.1175/1520-0450(1983)022%253C0537:PDIWHC%253E2.0.CO;2
- Minzner, R. A., Pond, H. L., & Champion, K. S. W. (1959). *The ARDC Model Atmosphere*, 1959. Geophysics Research Directorate, Air Force Cambridge Research Center, Air Research and Development Command, U.S. Air Force.
- Muñoz Sabater, J. (2019). ERA5-Land monthly averaged data from 1950 to present. Copernicus Climate Change Service (C3S) Climate Data Store (CDS). [Data set]. https://doi.org/10.24381/cds.68d2bb30
- Neev, D., & Emery, K. (1967). The Dead Sea, depositional processes and environments of evaporites. *Geol. Surv. Israel Bull*, 41, 147.
- Nehorai, R., Lensky, N., Brenner, S., & Lensky, I. (2013). The dynamics of the skin temperature of the Dead Sea. *Advances in Meteorology*, 2013.
- Nissenbaum, A. (1969). Studies in the geochemistry of the Jordan River-Dead Sea system. University of California, Los Angeles.
- Olson, K. J., Guillerm, E., Peaple, M. D., Lowenstein, T. K., Gardien, V., Caupin, F., Feakins, S. J., Tierney, J. E., Stroup, J., Lund, S., & McGee, D. (2023). Application of Brillouin thermometry to latest Pleistocene and Holocene halite from Searles Lake, California, USA. *Earth and Planetary Science Letters*, 602, 117913. https://doi.org/10.1016/j.epsl.2022.117913
- Oroud, I. M. (1995). Effects of salinity upon evaporation from pans and shallow lakes near the Dead Sea. *Theoretical and Applied Climatology*, *52*(3), 231–240.
- Oroud, I. M. (2019). Evaporites: Relative humidity control of primary mineral facies revisited. *Hydrological Processes*, *33*(3), 395–404. https://doi.org/10.1002/hyp.13334
- Oroud, I. M. (2023). The future fate of the Dead Sea: Total disappearance or a dwarfed hypersaline hot lake? *Journal of Hydrology*, *623*, 129816.
- Ouillon, R., Lensky, N. G., Lyakhovsky, V., Arnon, A., & Meiburg, E. (2019). Halite Precipitation From Double-Diffusive Salt Fingers in the Dead Sea: Numerical Simulations. *Water Resources Research*, *55*(5), 4252–4265. https://doi.org/10.1029/2019WR024818

- Parkhurst, D. L., & Appelo, C. A. J. (2013). Description of input and examples for PHREEQC version 3: A computer program for speciation, batch-reaction, one-dimensional transport, and inverse geochemical calculations (USGS Numbered Series Nos 6-A43; Techniques and Methods, Issues 6-A43, p. 519). U.S. Geological Survey. http://pubs.er.usgs.gov/publication/tm6A43
- Pilla, R. M., Williamson, C. E., Adamovich, B. V., Adrian, R., Anneville, O., Chandra, S., Colom-Montero, W., Devlin, S. P., Dix, M. A., Dokulil, M. T., Gaiser, E. E., Girdner, S. F., Hambright, K. D., Hamilton, D. P., Havens, K., Hessen, D. O., Higgins, S. N., Huttula, T. H., Huuskonen, H., ... Zadereev, E. (2020). Deeper waters are changing less consistently than surface waters in a global analysis of 102 lakes. *Scientific Reports*, 10(1), 20514. https://doi.org/10.1038/s41598-020-76873-x
- Radko, T. (2013). *Double-Diffusive Convection*. Cambridge University Press.
- Rimmer, A., Gal, G., Opher, T., Lechinsky, Y., & Yacobi, Y. Z. (2011). Mechanisms of long-term variations in the thermal structure of a warm lake. *Limnology and Oceanography*, 56(3), 974–988.
- Roveri, M., Flecker, R., Krijgsman, W., Lofi, J., Lugli, S., Manzi, V., Sierro, F. J., Bertini, A., Camerlenghi, A., & De Lange, G. (2014). The Messinian Salinity Crisis: Past and future of a great challenge for marine sciences. *Marine Geology*, 352, 25–58.
- Salhotra, A. M., Adams, E. E., & Harleman, D. R. (1985). Effect of salinity and ionic composition on evaporation: Analysis of Dead Sea evaporation pans. *Water Resources Research*, *21*(9), 1336–1344.
- Schmitt, R. W. (1981). Form of the Temperature-Salinity Relationship in the Central Water: Evidence for Double-Diffusive Mixing. *Journal of Physical Oceanography*, *11*(7), 1015–1026. https://doi.org/10.1175/1520-0485(1981)011%253C1015:FOTTSR%253E2.0.CO;2
- Schreiber, B. C., & El Tabakh, M. (2000). Deposition and early alteration of evaporites. *Sedimentology*, 47, 215–238.
- Scribano, V., Carbone, S., Manuella, F. C., Hovland, M., Rueslåtten, H., & Johnsen, H.-K. (2017). Origin of salt giants in abyssal serpentinite systems. *International Journal of Earth Sciences*, 106(7), 2595–2608.

- Sirota, I., Arnon, A., & Lensky, N. G. (2016). Seasonal variations of halite saturation in the Dead Sea. *Water Resources Research*, *52*(9), Article 9. https://doi.org/10.1002/2016WR018974
- Smith, S. D. (1988). Coefficients for sea surface wind stress, heat flux, and wind profiles as a function of wind speed and temperature. *Journal of Geophysical Research: Oceans*, 93(C12), 15467–15472.
- Smith, W. L. (1966). Note on the Relationship Between Total Precipitable Water and Surface Dew Point. *Journal of Applied Meteorology and Climatology*, *5*(5), Article 5. https://doi.org/10.1175/1520-0450(1966)005%253C0726:NOTRBT%253E2.0.CO;2
- Sonntag, D. (1990). Important new values of the physical constants of 1986, vapor pressure formulations based on the ITS-90, and psychrometer formulae. *Z. Meteorol.*, 70, 340–344.
- Stanhill, G. (1987). The radiation climate of the dead sea. *Journal of Climatology*, 7(3), Article 3. https://doi.org/10.1002/joc.3370070305
- Stanhill, G. (1990). Changes in the surface temperature of the dead sea and its heat storage. *International Journal of Climatology*, 10(5), Article 5.

 https://doi.org/10.1002/joc.3370100508
- Stanhill, G. (1994). Changes in the rate of evaporation from the Dead Sea. *International Journal of Climatology*, *14*(4), 465–471.
- Steinhorn, I. (1983). In situ salt precipitation at the Dead Sea. *Limnology and Oceanography*, 28(3), Article 3. https://doi.org/10.4319/lo.1983.28.3.0580
- Steinhorn, I., Assaf, G., Gat, J. R., Nishry, A., Nissenbaum, A., Stiller, M., Beyth, M., Neev, D., Garber, R., Friedman, G. M., & Weiss, W. (1979). The Dead Sea: Deepening of the Mixolimnion Signifies the Overture to Overturn of the Water Column. *Science*, 206(4414), Article 4414. https://doi.org/10.1126/science.206.4414.55
- Stiller, M., Lensky, N., & Gavrieli, I. (2018). Recent evolution of the dead sea chemical composition: 2005-2015. In *Geol. Surv. Isr.* Ministry of Energy.
- Stone, P. H., & Carlson, J. H. (1979). Atmospheric Lapse Rate Regimes and Their Parameterization. *Journal of the Atmospheric Sciences*, *36*(3), Article 3. https://doi.org/10.1175/1520-0469(1979)036%253C0415:ALRRAT%253E2.0.CO;2

- Tong, Y., Feng, L., Wang, X., Pi, X., Xu, W., & Woolway, R. I. (2023). Global lakes are warming slower than surface air temperature due to accelerated evaporation. *Nature Water*, *I*(11), 929–940. https://doi.org/10.1038/s44221-023-00148-8
- Turner, J. S. (1967). Salt fingers across a density interface. *Deep Sea Research and Oceanographic Abstracts*, 14(5), 599–611.
- Vickers, D., Mahrt, L., & Andreas, E. L. (2015). Formulation of the Sea Surface Friction Velocity in Terms of the Mean Wind and Bulk Stability. *Journal of Applied Meteorology and Climatology*, *54*(3), 691–703. https://doi.org/10.1175/JAMC-D-14-0099.1
- Wagner, W., & Pruss, A. (1993). International equations for the saturation properties of ordinary water substance. Revised according to the international temperature scale of 1990. Addendum to J. Phys. Chem. Ref. Data 16, 893 (1987). *Journal of Physical and Chemical Reference Data*, 22(3), 783–787.
- Wagner, W., & Pruß, A. (2002). The IAPWS Formulation 1995 for the Thermodynamic Properties of Ordinary Water Substance for General and Scientific Use. *Journal of Physical and Chemical Reference Data*, 31(2), Article 2. https://doi.org/10.1063/1.1461829
- Wang, J., & Lowenstein, T. K. (2017). Anomalously High Cretaceous Paleobrine Temperatures: Hothouse, Hydrothermal or Solar Heating? *Minerals*, 7(12), 245. https://doi.org/10.3390/min7120245
- Warren, J. K. (2010). Evaporites through time: Tectonic, climatic and eustatic controls in marine and nonmarine deposits. *Earth-Science Reviews*, *98*(3), Article 3. https://doi.org/10.1016/j.earscirev.2009.11.004
- Williams, D. R. (2024). *National Aeronautics and Space Administration Earth Fact Sheets*. https://nssdc.gsfc.nasa.gov/planetary/factsheet/earthfact.html
- Zhang, J., Schmitt, R. W., & Huang, R. X. (1998). Sensitivity of the GFDL Modular Ocean Model to Parameterization of Double-Diffusive Processes. *Journal of Physical Oceanography*, 28(4), 589–605. https://doi.org/10.1175/1520-0485(1998)028%253C0589:SOTGMO%253E2.0.CO;2
- Zilberman, T., Gavrieli, I., Yechieli, Y., Gertman, I., & Katz, A. (2017). Constraints on evaporation and dilution of terminal, hypersaline lakes under negative water balance: The

Dead Sea, Israel. Geochimica et Cosmochimica Acta, 217, 384–398.

https://doi.org/10.1016/j.gca.2017.08.040

Acknowledgments: We thank Nadav Lensky for fruitful discussions.

Funding:

European Union's Horizon 2020 research and innovation programme under the Marie Skłodowska-Curie grant agreement No 101029939 (EG, TKL, AB)

National Agency for Research in France, grant agreement No 2AZ52ACLIMS-Gardien (VG)

Author contributions:

Conceptualization: EG, FC, VG, TKL, AB

Methodology: EG, FC, FB, DB

Software: EG, FC

Investigation: EG

Validation: EG

Formal analysis: EG, FC

Resources: EG, TKL, AB

Visualization: EG

Data Curation: EG

Project administration: EG, TKL, AB

Funding acquisition: EG, TKL, AB

Supervision: EG, FC, VG, AB, TKL

Writing—original draft: EG

Writing—review & editing: EG, AB, VG, FB, TKL, DB, FC

Competing interests: Authors declare that they have no competing interests.

Supplementary Materials

Materials and Methods

Supplementary Text

Figs. S1 to S8

Tables S1 to S2

References (50–103)

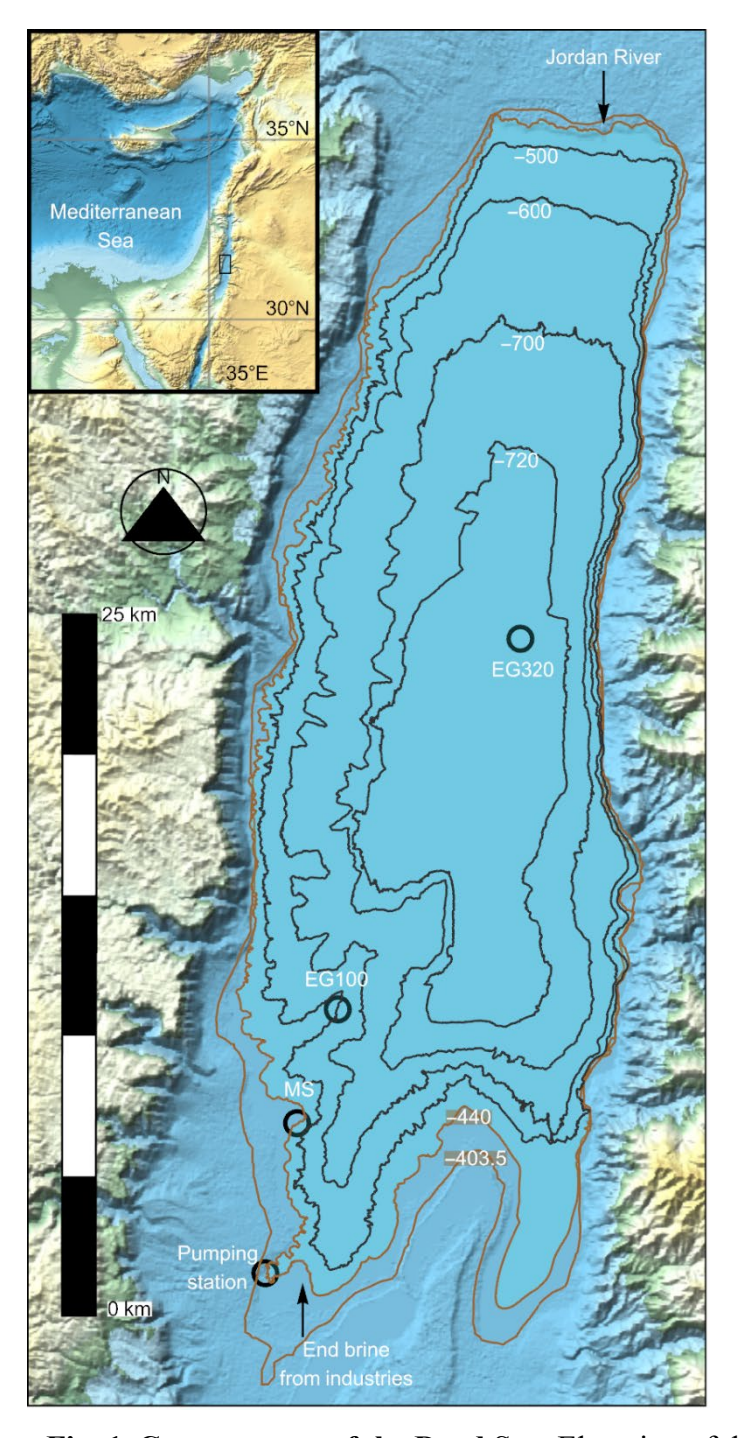


Fig. 1. Contour map of the Dead Sea. Elevation of the lake in 1985 (-403.5 m asl) and in 2024 (~-440 m asl) shown as brown lines. Monitoring stations mentioned in the text: MS 31°233'N, 35°251'E, -430 m asl; EG100 31°257'N, 35°262'E; EG320 31°342'N, 35°311'E. Inset shows Levant region in the eastern Mediterranean; black rectangle encloses the Dead Sea map.

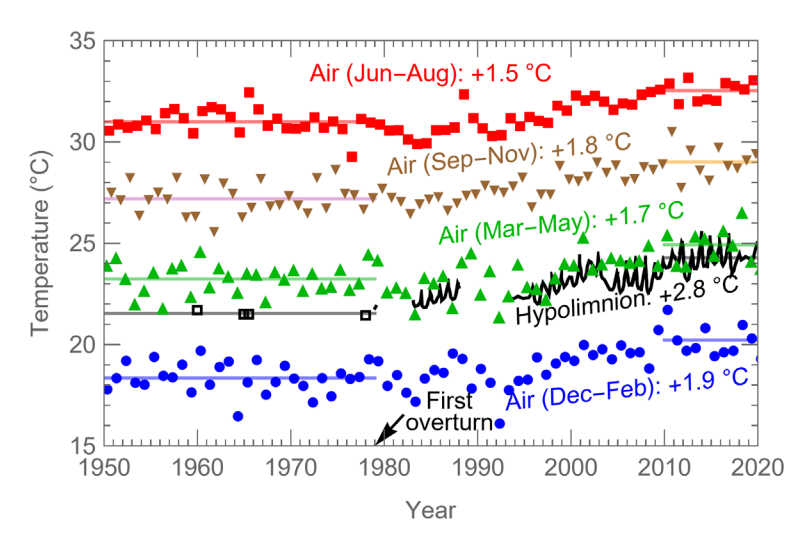


Fig. 2. Air and hypolimnion temperatures in the Dead Sea, 1950–2019. Warming is calculated as temperature difference between 2010–2019 and 1950–1978. Data source: (see *Materials and Methods*).

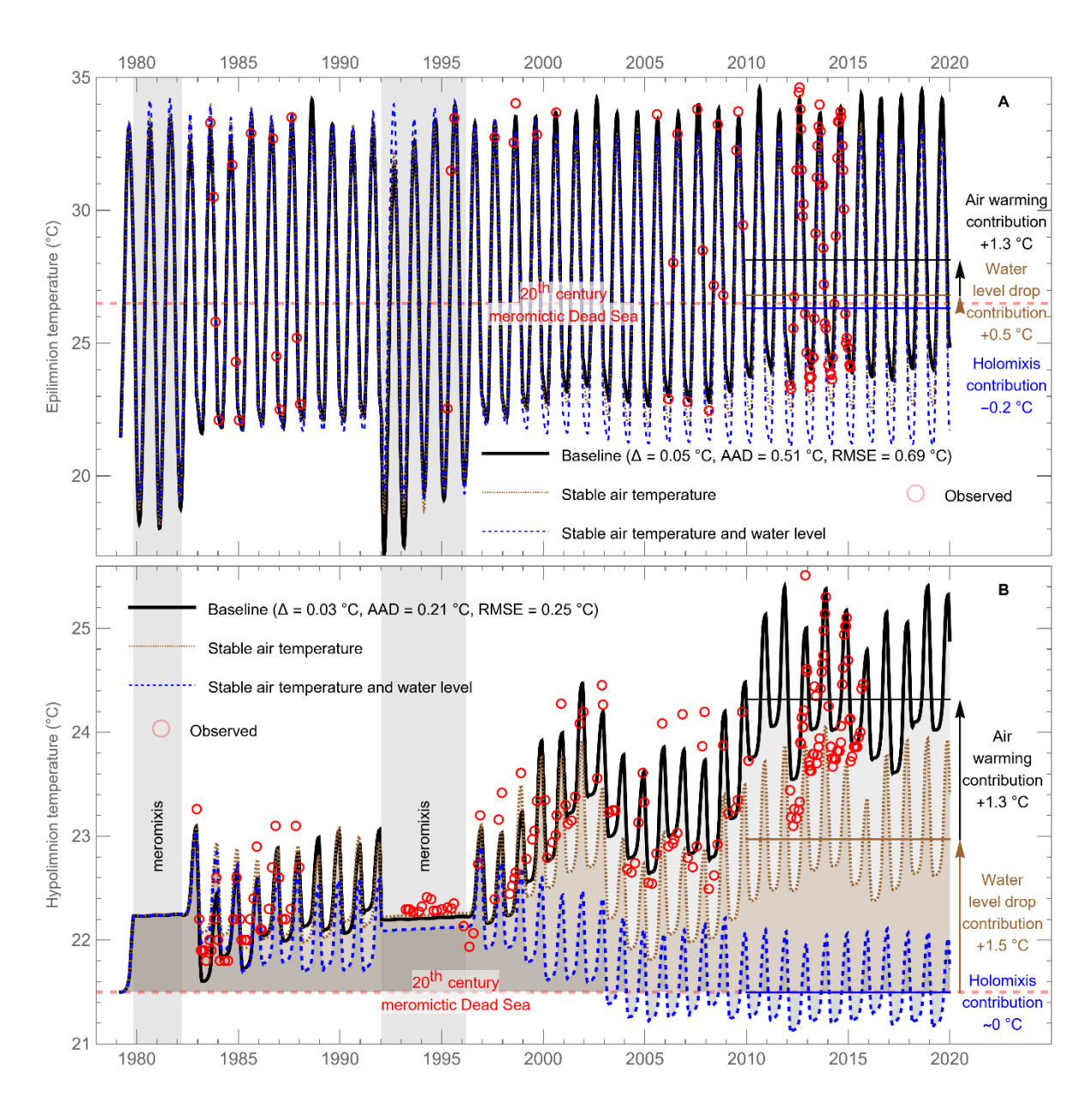


Fig. 3. Epilimnion (A) and hypolimnion (B) temperatures of the Dead Sea in the baseline simulation, in the sensitivity simulations and as measured at monitoring stations.

Epilimnion and hypolimnion temperature measurements are from water depth 7–15 m and \geq 50 m, respectively. Data source: (see *Materials and Methods*). Agreement between baseline simulation and measurements is indicated by mean bias (Δ), average absolute deviation (AAD) and root mean square error (RMSE).

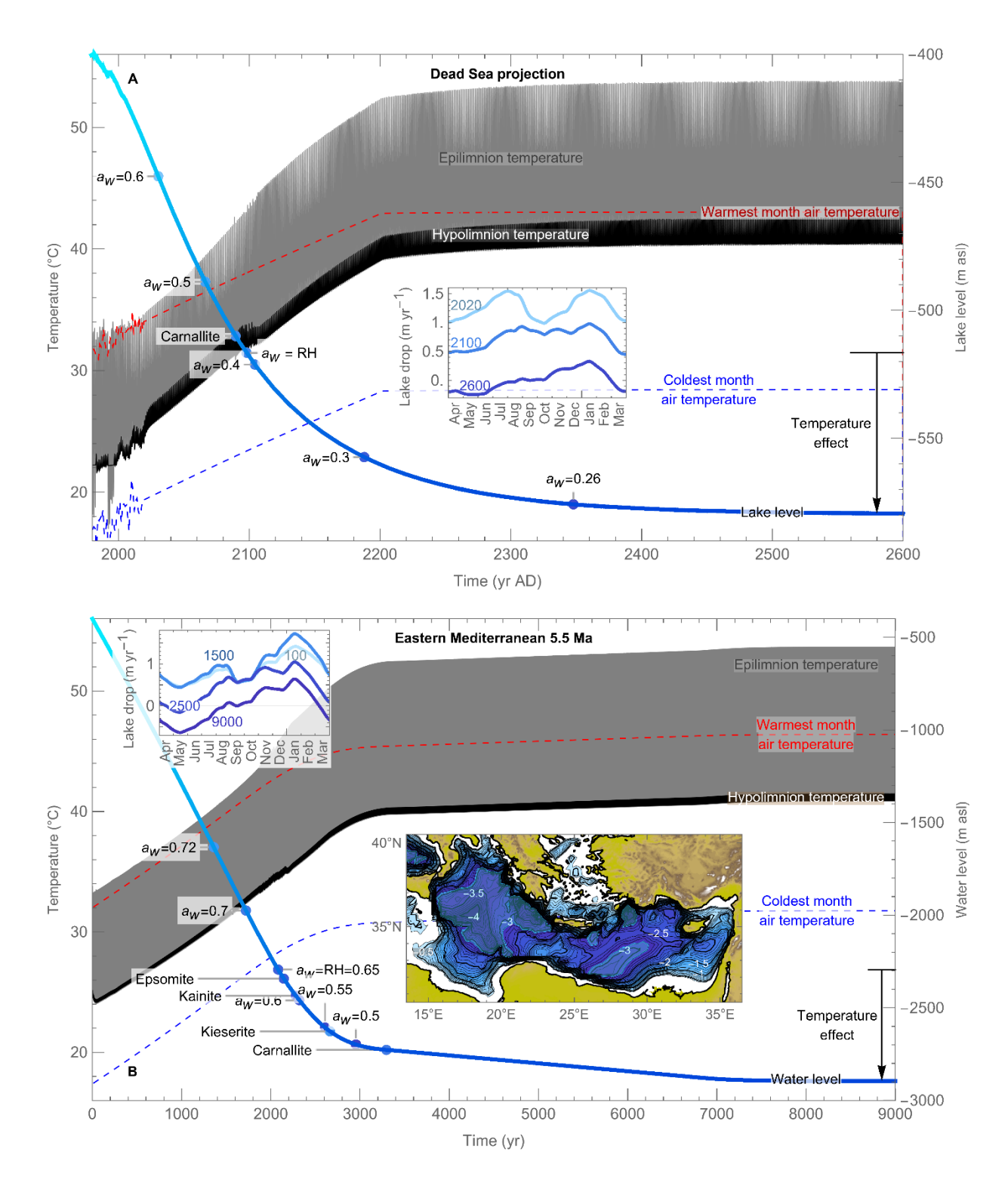


Fig. 4. Extreme warming and water level decline as simulated for the future Dead Sea and Messinian eastern Mediterranean Sea. (A) Lake level and water temperature in the Dead Sea projection (2019–2600) and baseline (1979–2019) simulations. Input air temperature increases

with anthropogenic air warming (+0.045 °C yr⁻¹ capped at +10 °C) and lapse rate (-5.8 °C km⁻¹). **(B)** Water level and water temperature in the Messinian eastern Mediterranean Sea simulation. Input air temperature increases with lapse rate (-5.8 °C km⁻¹). In the eastern Mediterranean map, elevation contours (white numbers, in km asl, with 0.1 km asl spacing) are shown up to -0.4 km asl, which is the simulation's initial water level. Blue surfaces at -2895 m asl show extent of the residual waterbody at end of simulation. (A,B) H₂O activity (*a*_w), major minerals of the evaporation sequence, and water level drop rate (insets) are shown at several simulation times to illustrate the evolution of the evaporation process. "Temperature effect" arrow indicates the amount of water level decline that occurred after *a*_w became smaller than relative humidity.

Supplementary Materials

Materials and Methods

The model setup is illustrated in Fig. S6, including seasonal average values of model output heat fluxes. Detailed equations, parameters and values of constants are given in Tables S1,2.

Model differential equations

The model has three modes: *holomictic stratified season*, *holomictic mixed season* and *meromictic*.

In holomictic stratified season mode, the model calculates the temperature of the epilimnion (T_e) and hypolimnion (T_h) by solving, with Mathematica's function NDSolve, the coupled ordinary differential equations

$$\frac{\mathrm{d}T_{\mathrm{e}}}{\mathrm{d}t} = \frac{A_{\mathrm{DS}} J_{\mathrm{surf}} - A_{\mathrm{h}} J_{\mathrm{D,T}}}{V_{\mathrm{e}} C_{\mathrm{p,w}}}$$
 (Equation 1)

and

$$\frac{dT_{h}}{dt} = \frac{A_{h} J_{D,T}}{V_{h} C_{D,W}}.$$
 (Equation 2)

 J_{surf} is the net heat flux at the air-water interface; $J_{\text{D,T}}$ is the diffusive heat flux from the epilimnion to the hypolimnion; V_{e} and V_{h} are the volume of the epilimnion and hypolimnion, respectively; A_{DS} and A_{h} are the area of the Dead Sea surface and of the thermocline, respectively; $C_{\text{p,w}}$ is the heat capacity of Dead Sea brine; and t is time. Eqs. 1,2 are solved from the onset of stratification, set to March 15, until the overturn, which is taken to occur when the modeled temperatures of the two water layers become equal.

In *holomictic mixed season* mode, the model calculates the temperature of the mixed Dead Sea (T_{DS}) by solving the ordinary differential equation

$$\frac{dT_{DS}}{dt} = \frac{A_{DS} J_{surf}}{V_{DS} C_{p,w}},$$
 (Equation 3)

where $V_{\rm DS}$ is the volume of the Dead Sea. Eq. 3 is solved from the overturn until March 15.

In *meromictic* mode, the model solves Eqs. 1,2 as in the *holomictic stratified season* mode. The difference is in the way $J_{D,T}$ is calculated: see below.

In the baseline and sensitivity simulations, the *meromictic* mode was prescribed for two periods, November 1, 1979–March 15, 1982 and January 15, 1992–March 15, 1996, based on observed

surface water density and lake level. The waterbody is assumed constantly holomictic in the Dead Sea projection and Mediterranean simulations.

In the case of the Dead Sea projection and eastern Mediterranean simulations one additional variable is solved: water level. The time derivative of water level is set equal to the opposite of the evaporation rate, thus assuming no inflow nor brine pumping.

Diffusive diapycnal heat fluxes

The model accounts for the diapycnal exchanges of heat between the epilimnion and the hypolimnion at the thermocline through Fourier's law

$$J_{\rm D,T} = C_{\rm p,w} K_{\rm T} \frac{T_{\rm e} - T_{\rm h}}{h_{\rm T}}$$
, (Equation 4)

with h_T the thickness of the thermocline and K_T the effective thermal diffusivity at the thermocline. K_T encompasses several processes of diapycnal thermal exchange: molecular diffusivity, turbulent mixing (mainly due to surface and internal waves) and double diffusion. The use of Fourier's law assumes a linear dependence of all these processes on the temperature gradient at the thermocline. Theory suggests instead a 4/3 power dependence of DD fingering on the salinity gradient (Turner, 1967), however in practice interfaces between layers are thicker than predicted, hampering the use of the 4/3 power law (Kunze, 2003). Fourier's law with calibrated effective diffusivity has proved a reliable alternative way to model diapycnal exchanges (Inoue et al., 2007; Merryfield et al., 1999; Zhang et al., 1998).

In *meromictic* mode, the strong stratification restricts vertical exchanges to molecular diffusion; in Eq. 4 we set $h_T = 10$ m and $K_T = \kappa_T$, the molecular diffusivity of heat in pure water. In *holomictic mixed season* mode, based on 9 cm-resolution temperature profiles from the Dead Sea (Arnon et al., 2016), we set the value of h_T at 20 m at the onset of stratification, linearly decreasing until September 1st down to 1 m, and staying at 1 m until the overturn. Various expressions have been developed for K_T and are reviewed in (Ashin et al., 2022). Here we use the expression of Schmitt (Schmitt, 1981) as it is limited to two calibration parameters:

$$K_{\rm T} = K_{\rm T,turbulence} + \frac{K_{\rm T,DD}}{R_{\rho} \left[1 + \left(\frac{R_{\rho}}{R_{\rho,c}}\right)^n\right]}$$
 (Equation 5)

The first and second right-hand-side terms of Eq. 5 account for turbulent diffusion and double diffusion, respectively. Our calibration of $K_{T,turbulence}$ and $K_{T,DD}$ is described in *Model calibration*. The density ratio is expressed as

$$R_{\rho} = \frac{-\beta_{\rm T} (T_{\rm e} - T_{\rm h})}{\beta_{\rm S} (S_{\rm e} - S_{\rm h})},$$
 (Equation 6)

with β_T and β_S the expansivity coefficients for temperature and salinity, respectively, and S_e and S_h the salinity of the epilimnion and hypolimnion, respectively. Double diffusion is active in the Dead Sea for $R_\rho < 2$ (Arnon et al., 2016), so we set a cutoff value $R_{\rho,c} = 2$; using power n = 32 allows a sharp transition whereby the double diffusive term becomes insignificant for $R_\rho > R_{\rho,c}$. Moreover, we set $R_\rho \ge 1$ because stratification becomes unstable below this value.

Epilimnion-hypolimnion salinity difference

Since salinity is not directly simulated by our model, we inferred the salinity difference (S_e - S_h) for each year in the baseline and sensitivity simulations based on water deficit during the stratified season, itself estimated from lake level change, as follows:

- (i) We calculated the stratified season lake level changes using linearly interpolated lake level data (Israel Hydrological Service, 2020).
- (ii) We attributed 70% of lake level drop to water deficit, assuming the remaining 30% results from brine extraction for potash production (see discussion in (Arnon et al., 2016)).
- (iii) We normalized this water deficit-related lake level change to the average lake level drop of the three reference years 2012–2014.
- (iv) Using monthly salinity data from these reference years (Arnon et al., 2016), we derived a reference annual salinity difference cycle (S_e S_h)_{ref} (Fig. S3).
- (v) We scaled $(S_e S_h)_{ref}$ by the normalized lake level change to obtain the annual $(S_e S_h)$ cycle.

In the Dead Sea projection and eastern Mediterranean simulations, $(S_e - S_h)$ is calculated the same way, except that water deficit-related water level changes are directly derived from modeled water levels.

We chose to express $(S_e - S_h)$ as a linear function of lake level change, rather than of epilimnion volume change, for the sake of simplicity. This simplification has little impact on the results, given the little variation of area from top to base of epilimnion in the studied cases.

Note that our approach is a simplification, as $(S_e - S_h)$ may be influenced by variations in brine pumping, halite precipitation and diapycnal salt fluxes. We expect however this approach to quantify reliably the amplitude of the annual cycles of $(S_e - S_h)$, especially in the Dead Sea projection and eastern Mediterranean simulations in which industrial brine pumping is absent, because the rise from annual minimum to maximum of $(S_e - S_h)$ occurs from the onset of stratification to peak summer when diapycnal heat flux and epilimnetic halite precipitation are negligible.

Surface heat fluxes

The net heat flux at the air-water interface is expressed

$$J_{\text{surf}} = J_{\text{R}} - J_{\text{L}} - J_{\text{S}}.$$
 (Equation 7)

The three right-hand-side terms of Eq. 7 are the net radiative, latent and sensible heat fluxes, respectively. We do not account for heat fluxes from inflow, lake floor and halite precipitation as they are negligible (Lensky et al., 2005; Stanhill, 1990). The net radiative heat flux decomposes to

$$J_{\rm R} = J_{\rm R,sol} + J_{\rm R,a}$$
 - $J_{\rm R,w}$, (Equation 8)

where the three right-hand-side terms are insolation (shortwave radiation) penetrating water, downwelling longwave radiation penetrating water, and upwelling longwave radiation emitted by water, respectively.

Surface water temperature (T_s)

The temperature T_s of the surface water controls the fluxes of latent heat, sensible heat and upwelling longwave radiation. T_s may differ from the bulk epilimnion temperature T_e (during stratified season and meromixis) or from the bulk lake temperature T_{DS} (during mixing season) due to the formation at the top of the water column of a pluri-metric warm layer during the day and of a sub-millimetric cool layer called "sea skin" (Fairall et al., 1996; Nehorai et al., 2013). No synchronous measurements of surface and bulk temperatures in the Dead Sea are available. Instead, to estimate the difference between T_s and T_e , or between T_s and T_{DS} , we first calculated

average monthly values of $T_{\rm s}$ from a timeseries of monthly-resolved measurements obtained at EG100 between April 2015 and March 2017 (Hamdani et al., 2018). Then, for each month, we calculated the difference between these average monthly values of $T_{\rm s}$ and measurements of water temperature at 10 m depth obtained during between March 2012 and November 2014 near EG100 (Arnon et al., 2016). The resulting 32 values of temperature difference yield an average of -0.7 °C, so we define $T_{\rm s} = T_{\rm e}$ - 0.7 K (stratified season and meromixis) and $T_{\rm s} = T_{\rm DS}$ - 0.7 K (mixing season).

H₂O activity

Computing of surface brine H₂O activity (a_w) differed between simulations.

For the baseline simulation, we calculated a_w from surface brine density data (see *Input data*) using a H₂O activity—density relationship based on chemical equilibria. We calculated this relationship with PhreeqC v.3 (Parkhurst & Appelo, 2013) by modeling the dilution and evaporation paths of a starting brine with 1978 Dead Sea composition (Beyth, 1980): 1.95 mol Na⁺, 0.22 mol K⁺, 2.03 mol Mg²⁺, 0.48 mol Ca²⁺, 7.10 mol Cl⁻, 0.07 mol Br⁻, and 1 kg H₂O. Mineral phases in equilibrium were halite and carnallite. The dilution path added up to ~20-fold water in 0.02 kg increments, while the evaporation path removed up to 50% water in 0.001 kg increments. We fitted a third-order polynomial of H₂O activity as a function of brine density to the simulated dataset (R² = 0.99999; MSE = 2.36 10^{-7} ; Max error of fit: 0.5%; range of validity: $1000-1300 \text{ kg m}^{-3}$):

$$a_w = 3.66242 - 9.24506 \ 10^{-3} \rho_w + 1.10907 \ 10^{-5} \rho_w^2 - 4.51029 \ 10^{-9} \rho_w^3$$
. (Equation 8)

For the eastern Mediterranean simulation, to obtain a relationship between $a_{\rm w}$ and relative water volume, we modeled with PhreeqC v.3 the evaporation path at 25 °C of a brine with composition of Messinian seawater (Brennan et al., 2013) (0.486 mol Na⁺, 0.011 mol K⁺, 0.048 mol Mg²⁺, 0.012 mol Ca²⁺, 0.565 mol Cl⁻, 0.026 mol SO₄²⁻ and 1 kg H₂O). Mineral phases in equilibrium were calcite, aragonite, gypsum, halite, epsomite, kainite, carnallite, bischofite, sylvite and kieserite. Evaporation was simulated by removing water in 0.001 kg increments up to halite saturation and then in 0.0001 kg increments until 99.99% of the water was removed. Relative water volume at each evaporation step was defined by dividing water volume by the water volume at the step when halite first precipitated. The $a_{\rm w}$ -relative water volume relationship was obtained by linear interpolation.

In all PhreeqC simulations, the *pitzer.dat* database was used, charge balance was accommodated by Cl⁻, simulation temperature and pressure were 25 °C and 1 atm. Mineral phases in equilibrium precipitated when supersaturated; they dissolved if undersaturated and until total consumption of the stock previously accumulated via precipitation.

Model calibration

We calibrated $K_{T,turbulence}$ and $K_{T,DD}$ by comparing modeled epilimnion and hypolimnion temperatures with monthly monitoring data from 2012–2015 (Arnon et al., 2016) (Fig. S3). First, we ran 400 simulations covering all 400 combinations of the two parameters from 0.5 10^{-6} m² s⁻¹ to $10 \cdot 10^{-6}$ m² s⁻¹ in 0.5 10^{-6} m² s⁻¹ increments. We then computed the RMSE for both water layers and identified the best-performing combination. Next, we refined the search by testing values within $\pm 1 \cdot 10^{-6}$ m² s⁻¹ of the initial minimum-RMSE pair, at 0.1 10^{-6} m² s⁻¹ steps. The final parameter set minimized the mean RMSE across both layers.

Input data

Unless stated otherwise, we describe here the input data of the baseline simulation.

Surface water density

We compiled surface water density at 25 °C from offshore station EG320 using three data sources covering 1980–1987 and 2000–2019 (2021), 1991–1993 (1993), and 1998–2000 (2002).

Gap-filling methods differed between holomictic and meromictic periods.

During holomictic periods, observed surface water density follows a consistent seasonal pattern—rising by 2–3 kg m⁻³ from spring to summer, then decreasing similarly in fall and winter—superimposed on a longer-term upward trend due to evaporative concentration. To fill gaps, we:

- Estimated the seasonal amplitude based on the average amplitude from years bordering each gap.
- Interpolated the annual mean using linear regression between the surrounding years.

During meromictic periods, the surface layer becomes significantly diluted and seasonal patterns are irregular. For these periods, we applied simple linear interpolation between available data points.

Surface air pressure

We used the average monthly surface air pressure data of 1992–2000 measured at offshore station EG100 (2003) which we adjusted for lake surface elevation following the hydrostatic relation of the ARDC standard atmosphere (Minzner et al., 1959).

Reanalysis data

We used ERA5-Land reanalysis data (Muñoz Sabater, 2019), from Copernicus Climate Data Store (Copernicus Climate Change Service (C3S), 2022), for the period 1950–2023 at 31.5°N, 35.5°E, including:

- 2m air temperature and dewpoint temperature,
- 10 m zonal and meridional components of wind speed
- Surface net solar radiation

We computed:

- Lapse rate-corrected 2 m air temperature by applying a lapse rate -0.0058 $^{\circ}$ m⁻¹ based on the difference of lake level from the 2005–2013 average
- 10 m wind speed u_{10} as the vector magnitude combining the zonal and meridional components
- 2 m relative humidity from air temperature and dewpoint using Sonntag's formulation (1990) and IAPWS95 for saturation vapor pressure (Wagner & Pruß, 2002).

Local observations

We used local station data from offshore site EG100 for 2005–2013:

- 3 m wind speed and surface insolation from (Kishcha et al., 2018),
- and 3 m relative humidity and air temperature from IOLR (IOLR, 2021), digitized from plots with unknown time resolution.

To create monthly means from IOLR data, we linearly interpolated digitized points before averaging.

Vertical adjustment of wind speed and relative humidity

To adjust local data to 10 m height—the elevation needed in the equations for sensible and latent heat fluxes—we applied:

- Wind speed adjustment: Wind speeds were adjusted using empirical oceanic factors (S. D. Smith, 1988), based on the difference in virtual potential temperature between the saturated surface and air at 10 m. We interpolated tabulated values to create a continuous function for heights between 2–10 m, wind speed between 2–16 m s⁻¹, and virtual potential temperature difference between -10–10°C.
- Relative humidity adjustment: We used the logarithmic humidity profile for a smooth surface (Brutsaert, 1982):

$$\frac{q_{10}}{q_z} = \frac{q_z + \frac{E \log \frac{z}{10}}{k u_* \rho_a}}{q_z} \text{(Equation S1)}$$

where q_{10} and q_z are the specific humidity (kg/kg) at height 10 m and z, respectively, E is the evaporation rate (kg m⁻² s⁻¹), k = 0.41, ρ_a is air density (kg m⁻³) and u_* is friction velocity (m s⁻¹), calculated as (2015):

$$u^* = (0.17 - 0.019 u_{10} + 0.0042 u_{10}^2 - 0.000084 u_{10}^3) h(R_b)$$
 (Equation S2)

Stability correction factor $h(R_b)$ (2015) and bulk Richardson number R_b (Jiménez et al., 2012) are calculated as:

$$h(Rb) = \begin{cases} (1 - 60 R_b)^{0.1}, & R_b \le 0 \\ (1 + 60 R_b)^{-0.2}, & R_b > 0 \end{cases}$$
(Equation S3)

$$R_{\rm b} = \frac{(\theta_{\rm v,10} - \theta_{\rm v,0}) g \, 10}{(T_a + 0.1) \, u_{10}^2}$$
, (Equation S4)

with T_a the temperature of the air and g gravitational acceleration. The virtual potential temperature at height z is (American Meteorological Society, 2024):

$$\theta_{\rm v,z} = T_z \left(\frac{P_0}{P_z}\right)^{2/7} (1 + 0.61 \, q_z)$$
 (Equation S5)

where T_z is the temperature at height z, P_0 is surface air pressure and P_z is air pressure at height z. The adjusted humidity ratio (Eq. S1) was then used to convert relative humidity from height z to 10 m.

Iterative adjustment procedure

Because evaporation rate and surface water temperature (needed for Eqs. S1–S5) are model outputs, we used an iterative approach:

- 1. Initial calibration simulation (2012–2015) and baseline simulation (1979–2019) used guessed estimates for evaporation and temperature to calculate wind and humidity at 10 m.
- 2. Model outputs were fed back into the equations to recalculate 10 m wind and humidity.
- 3. ERA5 data were adjusted using monthly correction factors, one per month per variable, such that 2005–2013 monthly means matched EG100 observations.

For relative humidity, ERA5 values at 2 m were adjusted directly to 10 m.

We repeated steps 1–3 for seven iterations until the surface temperature converged within 0.01 °C. Results are shown in Fig. S2.

Water temperature data

Epilimnion and hypolimnion temperature measurements used in the model data comparison are from water depth 7–15 m (Anati & Stiller, 1991; Arnon et al., 2016; Beyth et al., 1998; 1996, 1998, 2000, 2001; Stiller et al., 2018) and \geq 50 m (Anati & Stiller, 1991; Arnon et al., 2016; Gertman et al., 2010; Stiller et al., 2018), respectively.

For water temperature shown in Fig. 2, in order to show hypolimnion temperatures until 2020, we used data that we digitized from (IOLR, 2021), except datapoints older than 1979 that we took from (Neev & Emery, 1967; Nissenbaum, 1969; Steinhorn et al., 1979).

Supplementary Text

To better understand why the Dead Sea's hypolimnion temperature response to air warming is considerably larger than the worldwide lake average, we ran 12 sensitivity simulations—one for each month—using baseline input but fixing that month's air temperature at its 1950–1978 average. We then calculated the average 2010–2019 temperature difference of each simulation with the baseline (Fig. S7). For the epilimnion, the temperature difference is similar around -0.1 °C in all 12 cases. Conversely, for the hypolimnion, the temperature difference is large around -0.3 °C in simulations with fixed winter month air temperature, while near-zero in simulations with fixed summer month air temperature. This highlights the dominant and strong influence of winter air temperature on hypolimnion warming, which is driven by the unique mixing dynamics of the Dead Sea.

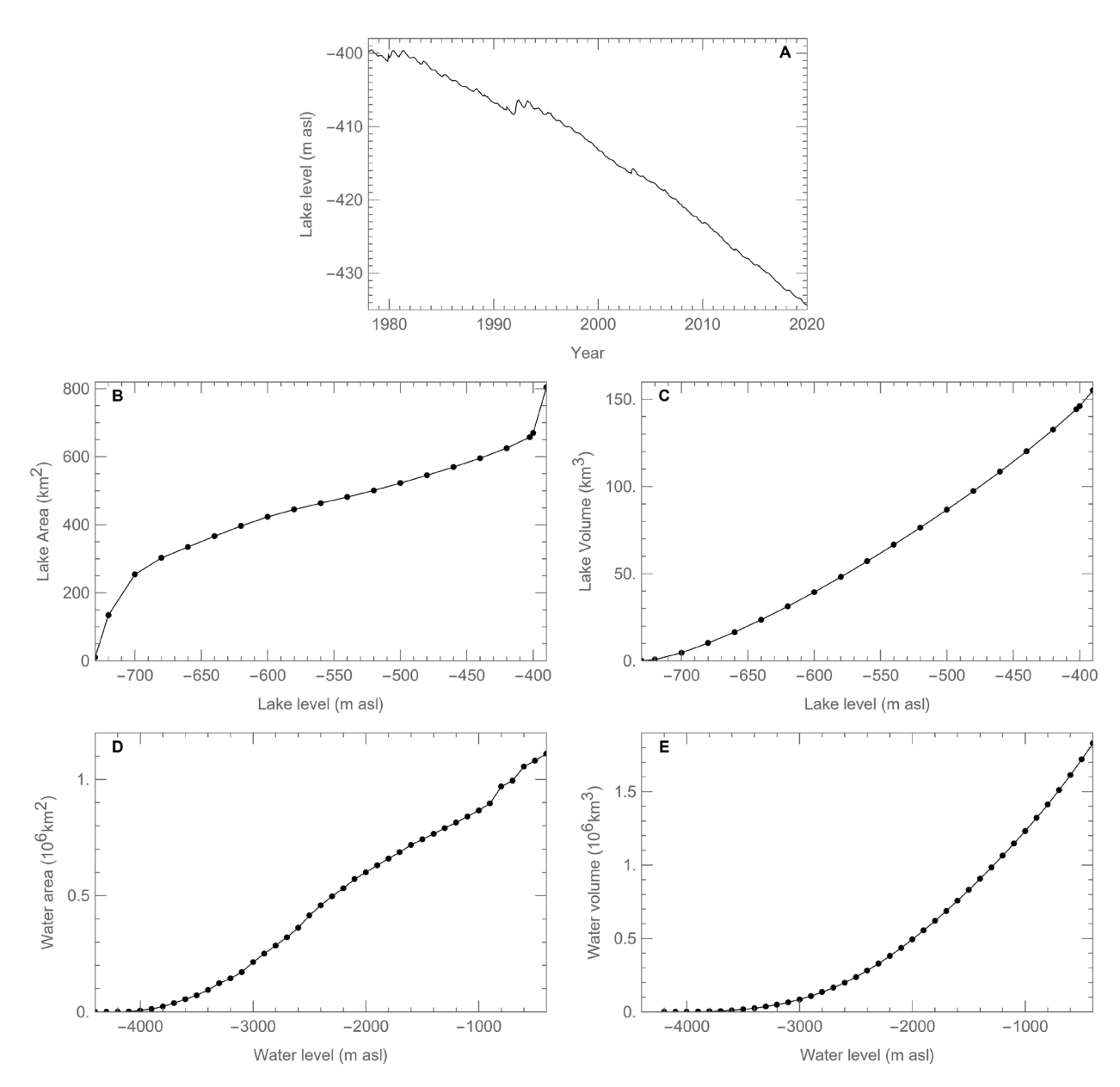


Fig. S1. Water level and hypsometry used in the model for the Dead Sea (A–C) and the eastern Mediterranean Sea (D,E). (A) Dead Sea lake level curve from (Israel Hydrological Service, 2020). (B) Dead Sea area—lake level relationship from (Guillerm et al., 2023) between -730 m asl and -420 m asl and from (Ben Dor et al., 2021) above -400 m asl. Datapoint at -402.5 m asl determined from intersection of the two linear interpolations. (C) Dead Sea Volume—Level relationship calculated by integration of the Area—Level relationship. (D) Eastern Mediterranean Sea Area—level relationship, calculated in this study using a digital elevation model with 40 km spatial resolution. The Strait of Sicily connecting eastern and western Mediterranean basins is

located slightly above -400 m asl in our digital elevation model. (E) Eastern Mediterranean Sea Volume–Level relationship calculated by integration of the Area–Level relationship.

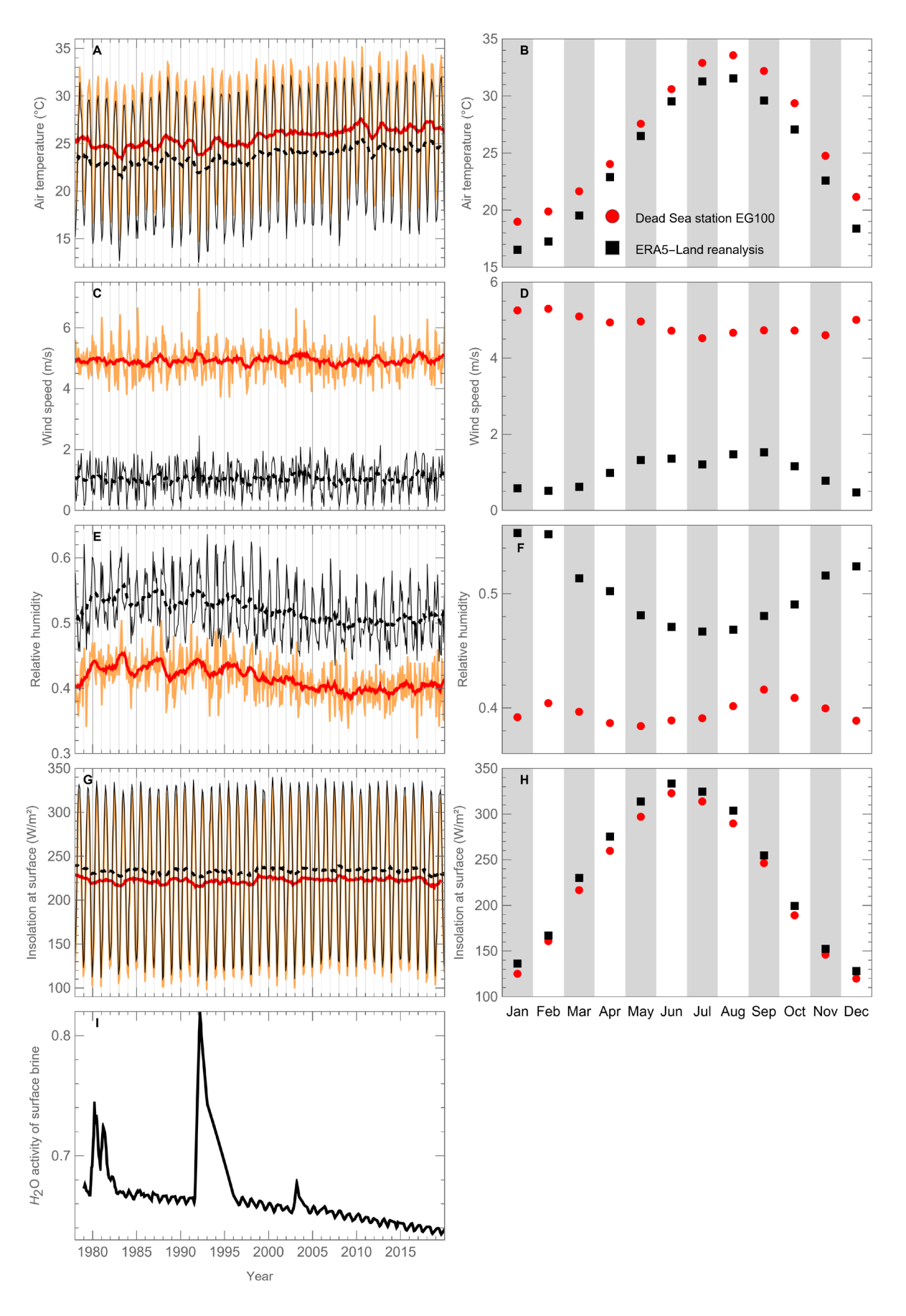


Fig. S2. Timeseries used in the baseline simulation. (A,C,E,G), ERA5-Land reanalysis data (black thin line) and calibrated input timeseries used in the model (orange line), along with their 12-month moving average (black dashed and red solid lines, respectively). (B,D,F,H), 2005–2013 monthly averages. For each month, the correction term used to adjust the ERA5-Land reanalysis timeseries is equal to the difference between the offshore station EG100 and the ERA5-Land reanalysis data. (I), H₂O activity of surface water calculated from surface water density.

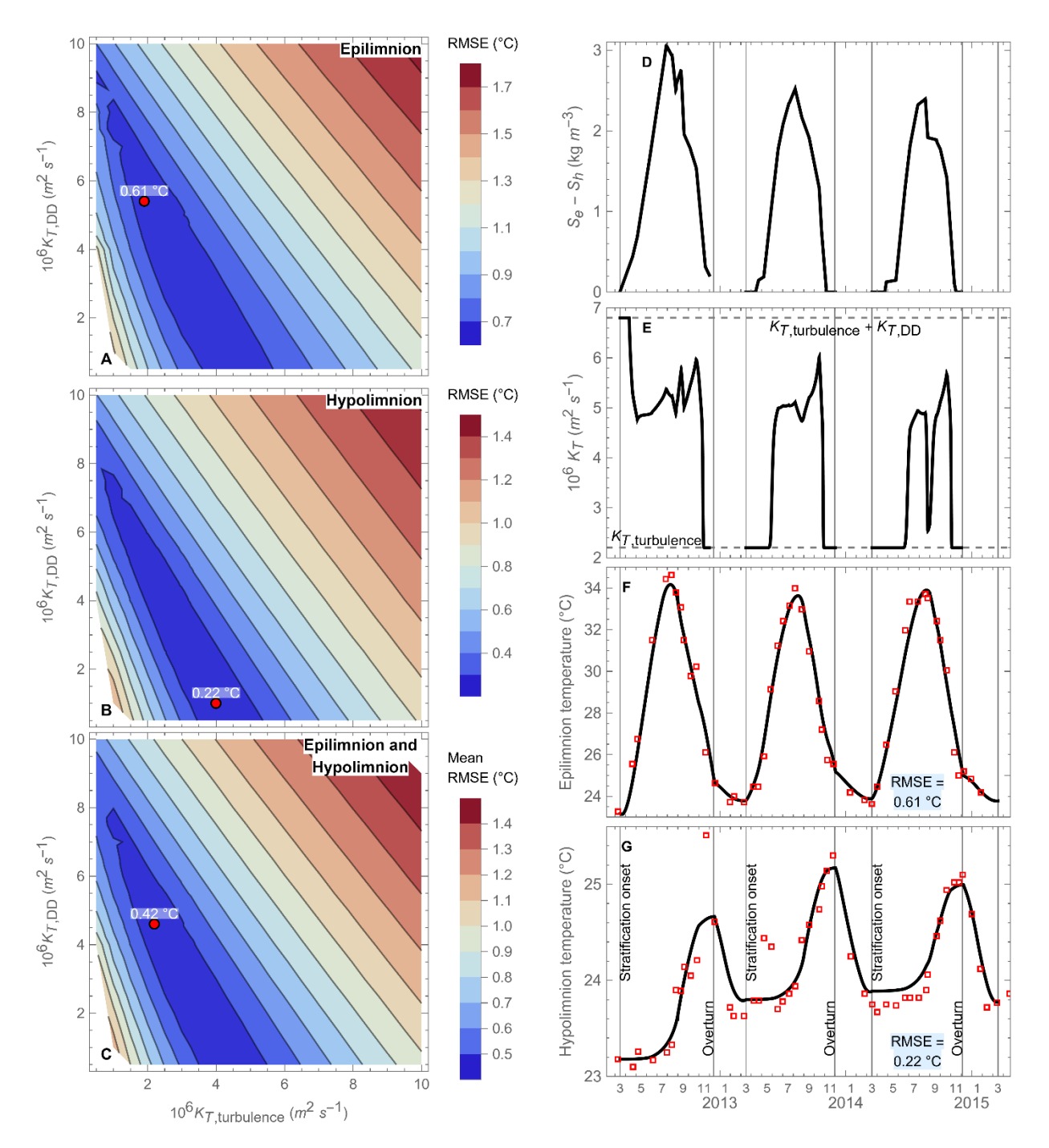


Fig. S3. Calibration of turbulent ($K_{T,turbulence}$) and double-diffusive ($K_{T,DD}$) heat diffusivities on reference years 2012–2015. A-C, Root mean square error (RMSE) of modeled epilimnion (**A**) and hypolimnion (**B**) temperatures, as well as mean RMSE of the two water layers (**C**), as a function of $K_{T,turbulence}$ and $K_{T,DD}$. Labeled red points show the lowest RMSE of the two water layers: $K_{T,turbulence} = 2.2 \cdot 10^{-6} \text{ m}^2 \text{ s}^{-1}$ and $K_{T,DD} = 4.6 \cdot 10^{-6} \text{ m}^2 \text{ s}^{-1}$. **D**, Linearly interpolated monitoring data of salinity difference between epilimnion and hypolimnion. **E**, Calculated effective diffusivity at the thermocline using best fit parameterization of diffusivities.

The value of K_T , bracketed between $K_{T,turbulence}$ and $(K_{T,turbulence} + K_{T,DD})$, increases when double diffusion is active, which depends on salinity and temperature gradients. **F-G**, Water temperature output in the case of the best fit parameterization of diffusivities. Temperature and salinity monitoring data from (Arnon et al., 2016).

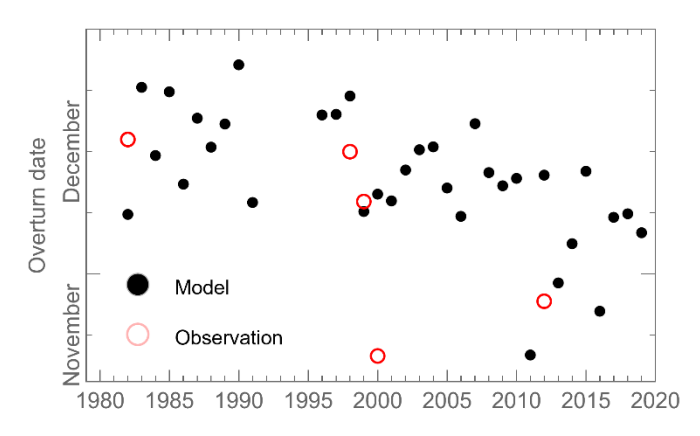


Fig. S4. Model-data comparison of overturn date. Observations from (Anati & Stiller, 1991; Arnon et al., 2016; Gertman & Hecht, 2002).

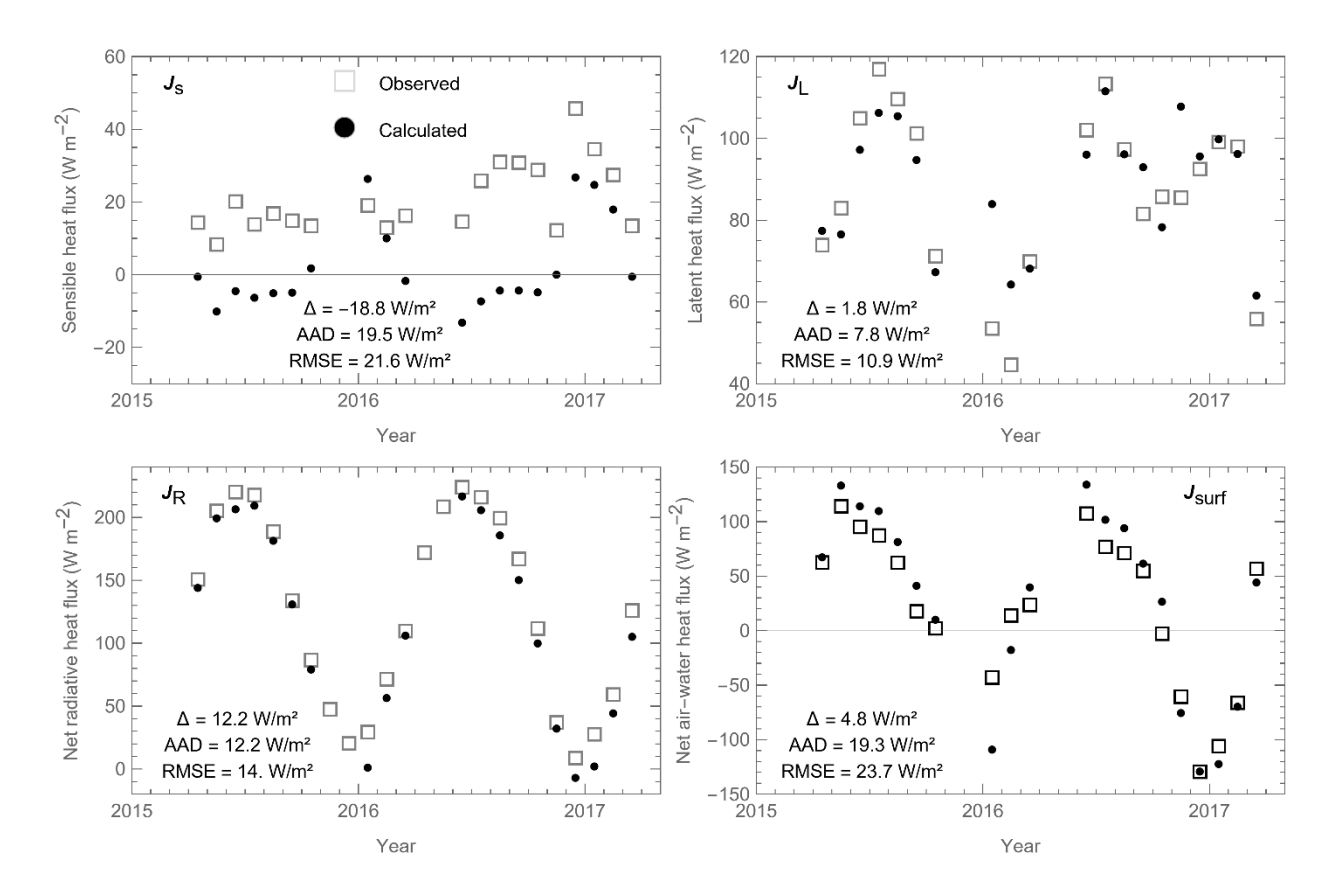


Fig. S5. Model-data comparison of heat fluxes. Measurements of sensible (J_S) and latent (J_L) heat fluxes are from shoreline station MS and net radiative heat flux $(J_R = J_{R,sol} + J_{R,a} - J_{R,w})$ is from offshore station EG100 (Hamdani et al., 2018). Net air—water heat flux is calculated as $J_{surf} = J_R - J_L - J_S$. For this model-data comparison, we calculated heat fluxes using climate data from these stations. We recalculated wind speed and relative humidity at 10 m above water surface based on atmospheric boundary layer theory. Modeled and observed J_{surf} agree closely due to the good agreement in the dominant components— J_R and J_L . In contrast, discrepancies in J_S have little effect on overall performance because of its minor contribution to J_{surf} .

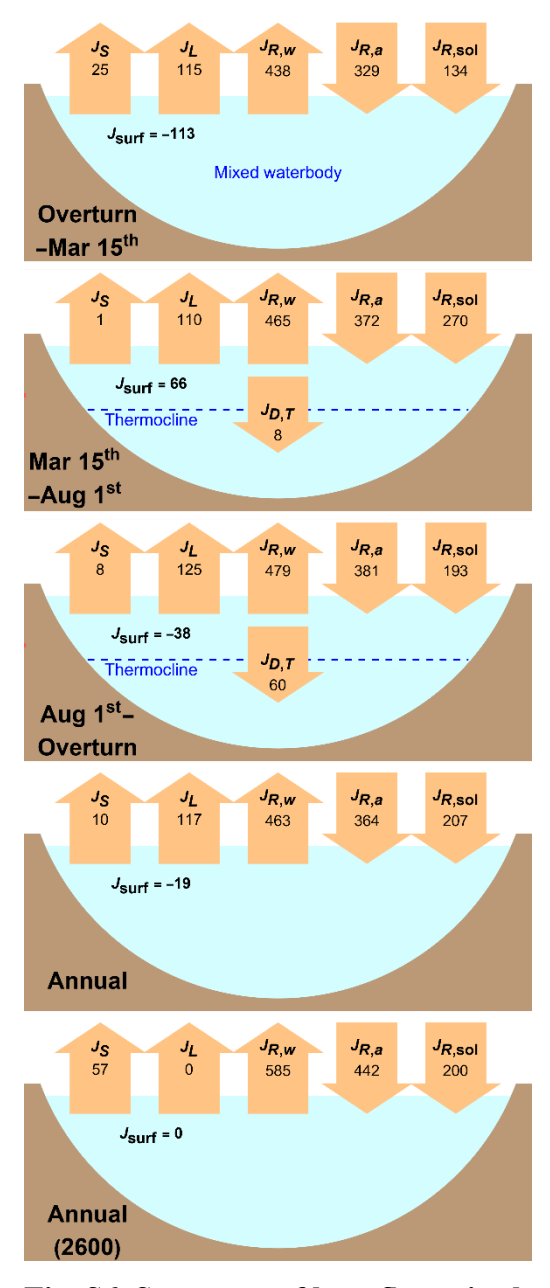


Fig. S6. Summary of heat fluxes in the Dead Sea simulations. Seasonal and annual heat fluxes (in W m⁻²) from the baseline simulation (1979–2019 average; 4 top graphs) and from the last year of the projection simulation (bottom graph). J_L : latent heat; J_S : sensible heat; $J_{R,w}$: upwelling longwave emissions from the water; $J_{R,a}$: downwelling longwave emissions from the air; $J_{R,sol}$: insolation penetrating water; J_{surf} : net heat flux at the air—water interface; $J_{D,T}$: effective heat diffusion at the thermocline. For calculation of surface-integrated fluxes, $J_{D,T}$ and the air—water heat fluxes must be multiplied by the thermocline area and the lake surface area, respectively. Note the net annual heat loss in the baseline simulation despite water warming, explained by the decrease in water volume.

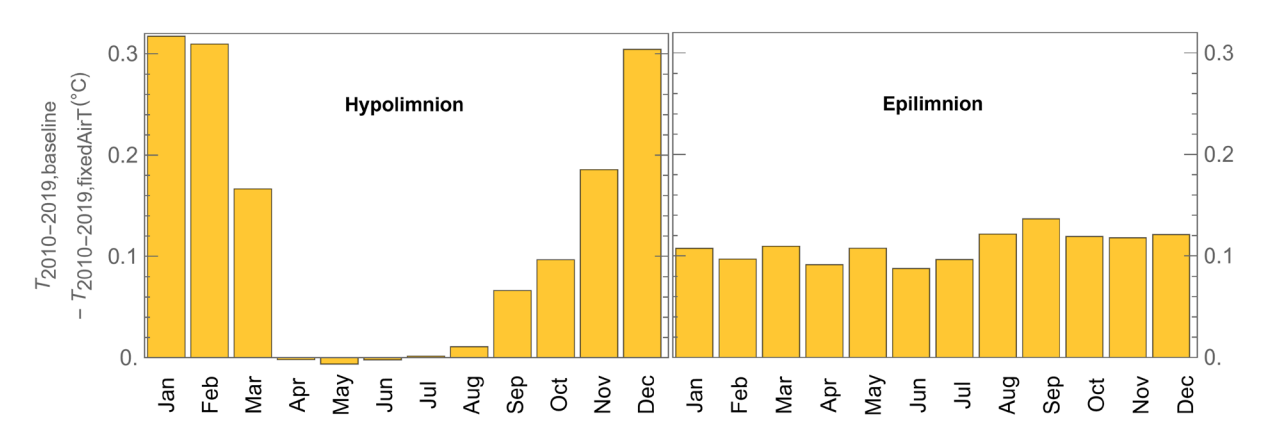


Fig. S7. Contribution of air warming in a given month to hypolimnion and epilimnion temperatures. The bar for each month shows the average 2010–2019 water temperature difference between the sensitivity simulation with air temperature of that one month fixed to its 1950–1978 mean and the baseline simulation.

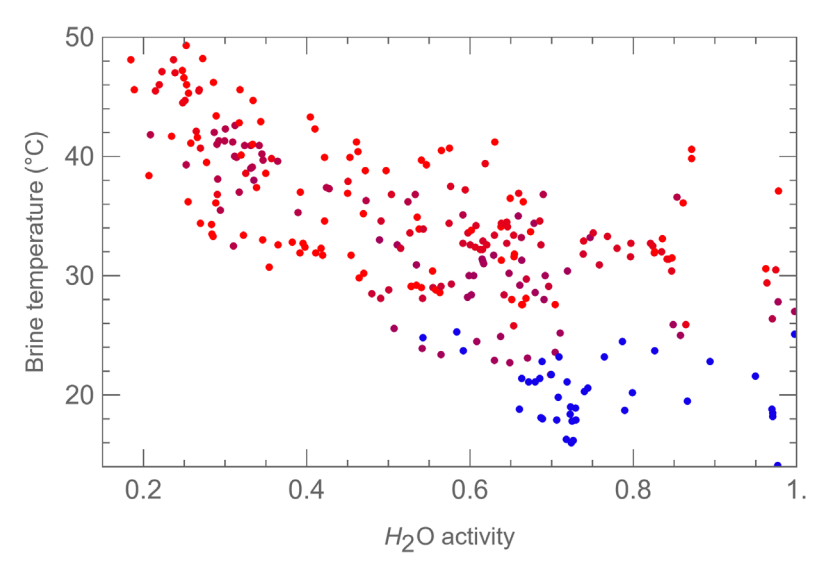


Fig. S8. Dependence of brine temperature on H₂O activity in brine pools around the Dead Sea. Brine pools around the Dead Sea fill thousands of sinkholes that have formed following the collapse of the underlying sediment into cavities in an ancient, regional salt layer. They range in diameter up to several tens of meters and reach depths of \sim 20 m. Their temperature and H₂O activity shown here was measured in 2006 and 2007 (Zilberman et al., 2017). Color indicates time of year, with red = 1st August and blue = 1st February).

Table S1 - Variables and constants.

Variable	Unit	Value	Remark	Reference
ar constant a _w		See text	Activity of H ₂ O at brine surface	
β_{T}	kg m ⁻³ K ⁻¹	0.45	Thermal expansion coefficient	(Anati, 1996)
β_{S}	kg m ⁻³ kg g ⁻	0.936	Salinity expansion coefficient	(Gertman et al., 2010)
$\mathcal{C}_{ ext{p,d}}$	J kg-1 K-1	1006	Dry air mass heat capacity	
$c_{ m p,v}$	J kg-1 K-1	1864	Water vapor mass heat capacity	
$C_{\mathrm{p,w}}$	J m ⁻³ K ⁻¹	3,740,000	Dead Sea volumetric heat capacity	(1990)
$arepsilon_{ m w}$		0.9955	Emissivity of surface water (annual average)	(1987)
е		0.01671	Earth's eccentricity	(2024)
$J_{ m R,sol,0}$	W m ⁻²	See text	Insolation at surface	
ΚΤ	m ² s ⁻¹	1.4 10-7	Molecular diffusivity of heat in water	
$K_{\mathrm{T,turbulence}}$	m ² s ⁻¹	2.2 10-6	Turbulent heat diffusivity at thermocline	Calibrated (this study)
$K_{\mathrm{T,DD}}$	m ² s ⁻¹	4.6 10-6	Double-diffusive heat diffusivity at thermocline	Calibrated (this study)
g	m s ⁻²	9.8	Gravitational acceleration	
φ	degrees	31.5	Latitude of the Dead Sea	
$M_{ m d}$	kg mol ⁻¹	0.02897	Molar mass of dry air	
$M_{ m v}$	kg mol ⁻¹	0.018015	Molar mass of water vapor	
ã	0	282.947	Earth's perihelion longitude + 180°	(2024)
Ω	0	23.44	Earth's axial tilt	(2024)
P_0	Pa	Input timeseries	Surface air pressure	
Pvap,sat*	Pa	611.213	Saturation vapor pressure at temperature T^*	(1993)
r	m	6,371,229	Earth's radius	
R	J K ⁻¹ mol ⁻¹	8.31446	Universal gas constant	
RH		Input timeseries	Relative humidity	
$ ho_{ ext{w}}$	kg m ⁻³	Input timeseries	Surface water density	
σ	W m ⁻² K ⁻⁴	5.67 10-8	Stefan-Boltzmann constant	
T	K		Temperature	
T^*	K	273.15	Standard temperature	
$T_{\rm a}$	K	Input timeseries	Air temperature at water surface	
$T_{a,pot}$	K	$T_{\rm a} + 0.1 \; {\rm K}$	Potential air temperature at 10 m height	(1988)
T_{DS}	K	Model output	Winter mixed waterbody temperature	
$T_{ m e}$	K	Model output	Epilimnion temperature	
$T_{ m h}$	K	Model output	Hypolimnion temperature	
$T_{ m s}$	K	${T_{\rm e} - 0.7}$ K, stratified lake ${T_{ m DS} - 0.7}$ K, mixed lake	Surface water temperature	
TSI _{AU=1}	W m ⁻²	1361	Total solar irradiance for Earth-Sun distance of	(2016)
u_z	m s ⁻¹	Input timeseries	Wind speed at height z	
Y	days	365.2422	Tropical year	

Table S2-Air-water heat flux equations. Subscript "0" refers to water surface.

Model parameter	Unit	Equation	Remarks	Reference
		Insolation		
$J_{ m R,sol}$	W m ⁻²	$(1-\alpha)$ $(1-\text{clf})$ $J_{\text{R,sol,clear,0}}$	Water-penetrating insolation	
α		$10^{-5} [21,348 - 525 (90 - \theta) + 4.1 (90 - \theta)^{2}]$	Water albedo (θ unit: °)	(Stanhill, 1987)
clf		$1 - \frac{J_{\rm R,sol,0}}{J_{\rm R,sol,clear,0}}$	Fraction of blocked insolation; right-hand-side fraction is the clearness index. Calculated with $J_{R,sol,0}$ measurements.	(1999)
$J_{ m R,sol,clear,0}$	W m ⁻²	$TSI\cos\theta X_{\mathrm{R}} X_{\mathrm{g}} X_{\mathrm{w}} X_{\mathrm{a}}$	Clear-sky insolation at water surface	(1983)
$X_{ m R}X_{ m g}$		$1.021 - 0.0854 \left[\frac{m_{\text{a}}}{m_{\text{a},\theta=0}} \left(\frac{P_0}{9.49 \cdot 10^6 \cdot \text{Pa}} + 0.051 \right) \right]^{0.5}$	Rayleigh scattering and gas absorption attenuation coefficient	(1974)
$X_{ m w}$		$1 - 0.039 \left(\frac{m_{\rm a}}{m_{\rm a, \theta=0}} \frac{PW}{1 \text{kg m}^{-2}} \right)^{0.3}$	Water vapor absorption attenuation coefficient	(1983)
Xa		$0.935 \frac{m_{\rm a}}{m_{\rm a,\theta=0}}$	Aerosol attenuation coefficient	(1983)
m _a	kg m ⁻²	$\rho_{\mathrm{a},0} \int_0^\infty \left(\frac{\rho_\mathrm{a}}{\rho_{\mathrm{a},0}}\right) \left[1 - \left(\frac{\sin\theta}{1 + \frac{h}{r}}\right)^2\right]^{-\frac{1}{2}} \mathrm{d}h$	Optical air mass, with $m_{a,\theta=0}$ the value for a vertical ray of light (h : elevation above water surface, meters).	(1965)
TSI	W m ⁻²	$\frac{\mathrm{TSI}_{\mathrm{AU}=1}}{{d_{\mathrm{SE}}}^2}$	Top-of-atmosphere total solar irradiance	(1983)
•		Downwelling longwave	radiation	
$J_{ m R,a}$	W m ⁻²	$J_{\text{R,a,clear}} * \left(1 - clf + \frac{clf}{\varepsilon_{\text{a,clear}}}\right)$	Flux of downwelling longwave radiation penetrating water	(Crawfor & Duchon 1999)
Ea,clear		$\frac{J_{ m R,a,clear}}{\sigma {T_{ m a}}^4}$	Clear-sky emissivity of atmosphere	
$J_{ m R,a,clear}$	W m ⁻²	$(1 \text{ W m}^{-2}) \left[59.38 + 113.7 \left(\frac{T_a}{T^*} \right)^6 + 96.96 \left(\frac{PW}{25 \text{ kg m}^{-2}} \right)^{0.5} \right]$	Clear-sky downwelling longwave radiation	(1998)
		Upwelling longwave ra	adiation	
$J_{R,\mathrm{w}}$	W m ⁻²	$\varepsilon_{\rm w} \sigma T_{\rm s}^{ 4} + (1 - \varepsilon_{\rm w}) J_{\rm R,a}$	Flux of upwelling longwave radiation emitted by the water surface	
		Sensible heat flux (con-	vection)	
$J_{ m S}$	W m ⁻²	$ \rho_{\rm a,0} \ c_{\rm p,a} \ C_{\rm T} \ u_{10} \left(T_{\rm s} - T_{\rm a,pot} \right) $	Flux of sensible heat from water surface.	(S. D. Smith, 1988)

C_{T}		$f(T_{\rm s}, u_{10})$	Transport coefficient. Interpolation of tabulated values from reference.	(S. D. Smith, 1988)
		Latent heat flux (evaporation,	condensation)	1700)
$J_{ m L}$	W m ⁻²	L E	Flux of latent heat from water surface	
L	J kg ⁻¹	$(10^{6} \mathrm{Jkg^{-1}}) \left(5.151 - 0.01395 \frac{T_{\rm s}}{1\rm K} + 1.6210^{-5} \left(\frac{T_{\rm s}}{1\rm K}\right)^{2}\right)$	Latent heat of vaporization (Dead Sea)	(2018)
Е	kg m ⁻²	$\frac{M_{\rm v}}{M_{\rm d}} \frac{\rho_{\rm a,0}}{P_0} \ 1.2 \ C_{\rm T} \ u_{10} (P_{\rm vap,w} - P_{\rm vap,a})$	Evaporation rate	(S. D. Smith, 1988)
		Astronomical funct	ions	
$d_{ m SE}$		$\frac{1 - e^2}{1 + e\cos(\lambda - \tilde{\omega})}$	Normalized Sun-Earth distance	
θ	rad	$\cos^{-1} \left[\sin \varphi \sin \delta + \cos \varphi \cos \delta \cos \left(\frac{\pi}{12} \right) \right]$ $-t)$	Solar zenith angle (t: time of day, in hours)	
δ	rad	$\sin^{-1}(\sin\Omega\sin\lambda)$	Solar declination	
λ	rad	$\lambda_{\rm m} + (2e - 0.25e^3)\sin(\lambda_{\rm m} - \tilde{\omega}) + \\ 1.25e^2\sin[2(\lambda_{\rm m} - \tilde{\omega})] + \frac{13}{12}e^3\sin[3(\lambda_{\rm m} - \tilde{\omega})]$	Earth's true longitude	(1978)
λ_{m}	rad	$\lambda_{\mathrm{m,VE}} + \Delta \lambda_{\mathrm{m}}$	Earth's mean longitude	(1978)
$\lambda_{ ext{m,VE}}$	rad	$-2\left[(0.5e + 0.125e^{3})\left(1 + (1 - e^{2})^{\frac{1}{2}}\right)\sin(-\tilde{\omega}) - 0.25e^{2}\left(0.5 + (1 - e^{2})^{\frac{1}{2}}\right)\sin(-2\tilde{\omega}) + 0.125e^{3}\left(\frac{1}{3} + (1 - e^{2})^{\frac{1}{2}}\right)\sin(-3\tilde{\omega})\right]$	Earth's mean longitude at vernal equinox (i.e. March 21, when $\lambda = 0$)	(2013)
$\Delta \lambda_m$	rad	$\frac{2\pi N}{Y}$	N: number of days from March 21.	
		Air and vapor		
$ ho_{ m a}$	kg m ⁻³	$\rho_{\rm a,0} \left(\frac{T_{\rm a}}{T_{\rm a} + \gamma \ h}\right)^{1 + \frac{g \ M_{\rm d}}{R \ \gamma}}$	Air density (h: elevation above water surface, meters)	(1959)
$ ho_{ ext{a,0}}$	kg m ⁻³	$\frac{M_{\rm d}\left(P_0 - P_{\rm vap,a}\right) + M_{\rm v} P_{\rm vap,a}}{R T_{\rm a}}$	Air density at water surface	
$P_{\mathrm{vap,a}}$	Pa	$RH P_{\mathrm{vap,sat}}(T_{\mathrm{a,pot}})$	Water vapor pressure at 10 m height	
$P_{ m vap,w}$	Pa	$a_{\rm w} P_{\rm vap,sat}(T_{\rm s})$	Water vapor pressure at water surface	
$P_{ m vap,sat}$	Pa	$22.064 \ 10^{6} \ \text{Exp} \left[\frac{^{647.066 \ \text{K}}}{^{7}} \left(-7.86\tau + 1.844\tau^{1.5} - 11.79\tau^{3} + 22.68\tau^{3.5} - 15.96\tau^{4} + 1.801\tau^{7.5} \right) \right]$	Saturation vapor pressure	(Wagner & Pruss, 1993)

w		$\frac{M_{\rm v}}{M_{\rm d}} \frac{P_{\rm vap,a}}{P_0 - P_{\rm vap,a}}$	Water vapor mixing ratio	
C _{p,a}	J kg ⁻¹ K ⁻	$\frac{c_{\rm p,d} + w c_{\rm p,v}}{1 + w}$	Air mass heat capacity	
		$1 - \frac{T}{647.096 \text{ K}}$		(Wagner & Pruss,
τ				1993)
$T_{ m d}$	K	(243.12 K) $\frac{\log \frac{P_{\text{vap,a}}}{P_{\text{vap,sat}}^*}}{17.62 - \log \frac{P_{\text{vap,a}}}{P_{\text{vap,a}}^*}}$	Dewpoint temperature	(1990)
γ	K m ⁻¹	$6.1910^{-3} + 4.5510^{-6}\varphi - 5.0310^{-7}\varphi^2$	Mean tropospheric lapse rate (Northern	Fit of data
			hemisphere)	from (1979)
		$10 \exp \left[-17.9517 - \log[B+1]\right]$	Atmosphere precipitable water. <i>B</i> is a	
PW	kg m ⁻²	$10 \text{ Exp} \left[-17.9317 - \log[B + 1] \right]$	function of time of year and latitude,	(1966)
		$+\ 0.07074\left(\frac{T^*}{K} + \frac{T_{\rm d}}{K}\right)\right]$	linearly interpolated from tabulated values	
			from reference.	